


## Article

# Innovative Remote Sensing Identification of Cyanobacterial Blooms Inspired from Pseudo Water Color

Zhen Cao <sup>1,2</sup> , Yuanyuan Jing <sup>1,2</sup>, Yuchao Zhang <sup>1,3,\*</sup>, Lai Lai <sup>1,2</sup>, Zhaomin Liu <sup>1,2</sup> and Qiduo Yang <sup>1,2</sup>

<sup>1</sup> Key Laboratory of Watershed Geographic Sciences, Nanjing Institute of Geography and Limnology, Chinese Academy of Sciences, Nanjing 210008, China

<sup>2</sup> University of Chinese Academy of Sciences, Beijing 100049, China

<sup>3</sup> Jiangsu Collaborative Innovation Center of Regional Modern Agriculture & Environmental Protection, Huaiyin Normal University, Huai'an 223300, China

\* Correspondence: yczhang@niglas.ac.cn; Tel.: +86-25-8688-2165

**Abstract:** The identification and monitoring of cyanobacterial blooms (CBs) is critical for ensuring water security. However, traditional methods are time-consuming and labor-intensive and are not ideal for large-scale monitoring. In operational monitoring, the existing remote sensing methods are also not ideal due to complex surface features, unstable models, and poor robustness thresholds. Here, a novel algorithm, the pseudo-Forel-Ule index (P-FUI), is developed and validated to identify cyanobacterial blooms based on Terra MODIS, Landsat-8 OLI, Sentinel-2 MSI, and Sentinel-3 OLCI sensors. First, three parameters of P-FUI, that is, brightness  $Y$ , saturation  $s$ , and hue angle  $\alpha$ , were calculated based on remote sensing reflectance. Then, the robustness thresholds of the parameters were determined by statistical analysis for a frequency distribution histogram. We validated the accuracy of our approach using high-spatial-resolution satellite data with the aid of field investigations. Considerable results were obtained by using water color differences directly. The overall classification accuracy is more than 93.76%, and the user's accuracy and producer's accuracy are more than 94.60% and 94.00%, respectively, with a kappa coefficient of 0.91. The identified cyanobacterial blooms' spatial distribution with high, medium, and low intensity produced consistent results compared to those based on satellite data. Impact factors were also discussed, and the algorithm was shown to be tolerant of perturbations by clouds and high turbidity. This new approach enables operational monitoring of cyanobacterial blooms in eutrophic lakes.

**Keywords:** cyanobacterial blooms; P-FUI; Lake Taihu; satellite data; monitoring



**Citation:** Cao, Z.; Jing, Y.; Zhang, Y.; Lai, L.; Liu, Z.; Yang, Q. Innovative Remote Sensing Identification of Cyanobacterial Blooms Inspired from Pseudo Water Color. *Remote Sens.*

**2023**, *15*, 215. <https://doi.org/10.3390/rs15010215>

Academic Editor: Junsheng Li

Received: 15 November 2022

Revised: 27 December 2022

Accepted: 27 December 2022

Published: 30 December 2022



**Copyright:** © 2022 by the authors. Licensee MDPI, Basel, Switzerland. This article is an open access article distributed under the terms and conditions of the Creative Commons Attribution (CC BY) license (<https://creativecommons.org/licenses/by/4.0/>).

## 1. Introduction

Cyanobacterial blooms (CBs) usually refer to blooms where cyanobacteria form floating scum with a blue-green color on the water surface. These blooms have experienced a period of dramatic global growth in recent decades due to nutrient loading and climate factors (e.g., temperature, rainfall, and solar radiation) [1–4]. The global exacerbation of CB conditions seriously threatens human health [5–8] and restricts socioeconomic development [9]. With significant public health concerns and socioeconomic development issues concerning water quality, it has been deemed necessary to implement early detection and effective monitoring of the reduction in CB intensity [10].

Traditional CBs monitoring requires regular sampling in representative areas and subsequent microscopy for identification and analysis (e.g., chlorophyll at concentration  $>20 \mu\text{g/L}$  or phytoplankton biovolume  $>5.0 \times 10^7 \text{ cells/L}$ ), the feasibility of which has been well documented [11–13]. However, these methods have limitations, such as the labor and time involved in sample acquisition over large spatial scales, the high costs of laboratory-based preparation and analysis, escalating expenses for personnel and equipment, and poor timeliness [14]. It is also challenging to obtain the spatial distribution characteristics and time-series variation of CBs [15]. After decades of rapid development, remote sensing

technology, with its broader monitoring range, faster imaging speed, shorter return period, and real-time dynamics, is believed to act as a countermeasure against these weaknesses of traditional monitoring methods and has become an important method for monitoring CBs, especially in large water bodies [16–22].

In general, the identification of CBs by remote sensing is based on significant water color variations, such as the greening of water mainly caused by CBs [2]. These changes are caused by the different spectral characteristics of pigments in cyanobacteria; for example, as indicators of cyanobacteria, phycocyanin has an absorption peak at 630 nm, while chlorophyll has a peak in reflectance at 550 nm and a trough at 665 nm [23,24]. Therefore, in operational monitoring, CBs are usually rendered a characteristic green color different to surrounding features by synthesizing false-color remote sensing images and then subjected to visual interpretation [25,26]. Similar spectral characteristics between CBs and aquatic/terrestrial plants often make it difficult to distinguish the two by visual inspection [27]. In order to improve the objectivity and stability of interpretation, remote sensing indices, especially the vegetation index, were used to identify CBs automatically, with increasing popularity [20,28].

CBs identification based on remote sensing technology has been studied extensively, including simple band algorithm, decision trees, mixed pixel decomposition, supervised/unsupervised classification, and algae-associated indices (see Table 1). Ratios of band reflectance and simple band transformations (e.g., simple band algorithm, algae-associated indices) are based on spectral characteristics for features detection but with the problems of similar spectral characteristics [27], while ensemble models (e.g., decision trees) often improved the error rate but with more complex structures [29,30]. These methods were designed to improve the accuracy of identifying CBs and to enable operational monitoring [31,32]. However, the results of the identification of CBs tend to be unsatisfactory in practice due to the varying quality of satellite data and the poor robustness of thresholds. At the same time, they are also severely susceptible to interference from factors such as clouds, aquatic vegetation, and highly turbid water bodies [26]. Therefore, identifying CBs based on remote sensing technology still requires further research; for example, the development of universal algorithms [15].

Specific band combinations based on satellite images could make CBs present different colors from the surrounding water surface. For example, CBs usually present yellow-green on true color images, and they present bright green on false color images (RGB: SWIR/NIR/Red) (Figure 1). Since the colors of CBs can be easily distinguished on false color maps, the pseudo-Forel-Ule index (comprising brightness  $Y$ , saturation  $s$ , and hue angle  $\alpha$ ) was proposed based on Terra MODIS (B7-B2-B1), Landsat-8 OLI (B7-B5-B2), Sentinel-2 MSI (B11-B8-B1), and Sentinel-3 OLCI (B8-B20-B6). Then, the P-FUI decision tree with robust thresholds was constructed to identify CBs. This method improved the accuracy and consistency of CBs monitoring, and considerable results were acquired mainly due to using water color differences directly. The main aim of this study was to provide important theoretical and technical support for the identification of CBs in eutrophic lakes, along with making progress in terms of its actual operational monitoring.

**Table 1.** Examples of CBs identification algorithms and their application area.

Algorithm Form	Reference	Application Area	Data Source
Simple band algorithm			
$R_{rs}(840)$	[33]	Clear Lake, USA	Airborne image
$R_{rs}(858.5)$ and $R_{rs}(858.5) / R_{rs}(555)$	[34]	Lake Taihu, China	MODIS
Red tide = $f(R_{rs}(912.5) / R_{rs}(615))$	[35]	West Coast, Canada	AVHRR
$R_{rs}(555)$ or $R_{rs}(680)$	[36]	East Sea, Korea peninsula	GOCI
Decision trees			
$TWI \geq CMI \geq FAI$	[27]	Lake Taihu, China	MODIS
$SD \geq TP \geq pH \geq DIN$	[37]	48 ponds, Belgium	In situ
$CSI \geq PBL$	[38]	156 lakes, USA	MERIS
$CI \geq ABM \geq \text{Median, Sen's slope, and Kendall's } \tau$	[39]		
Mixed pixel decomposition	[40]	Lake Taihu, China	MODIS
Algae pixel-growing algorithm	[41]	Lake Dianchi, China	GOCI
Linear mixing model	[42]	Part of Yellow Sea	HJ-1B
Improved N-FINDR	[43]		
Supervised/Unsupervised Classification			
ISODATA clustering	[44]	Moreton Bay, Australia	ETM+
Minimum distance classification	[45]	Lake Chaohu, China	MODIS
Maximum likelihood classification	[31]	North Sea, Netherlands	SeaWiFS
Algae-associated indices			
Floating algae index	[26]	Western Yellow Sea	MODIS
Forel-Ule index	[46]	Global Inland Waters	OLI
Chlorophyll-a	[47]	5 Lakes/Reservoirs, China	MSI
Visual cyanobacteria index	[48]	Ganga River, India	OLCI
NDVI, EVI	[49]	3 Lakes, Japan	ETM+
Machine learning			
Neural networks	[50]	Bohai Bay, China	AVHRR
Random forest	[51]	Han river, South Korea	In situ
Support vector machine	[52]	Sea Coast near Florida, USA;	MODIS
Long short-term memory		Arabian Gulf	GEBCO

Rrs: remote sensing reflectance; NDVI: normalized difference vegetation index; EVI: enhanced vegetation index; FAI: floating algae index; CMI: cyanobacteria and macrophytes index; TWI: turbid water index; DIN: dissolved inorganic nitrogen; SD: Secchi depth; TP: total phosphorus; PBL: baseline of phycocyanin [38,53]; CSI: chlorophyll spectral index [54]; ABM: annual bloom magnitude; CI: cyanobacteria Index [55].

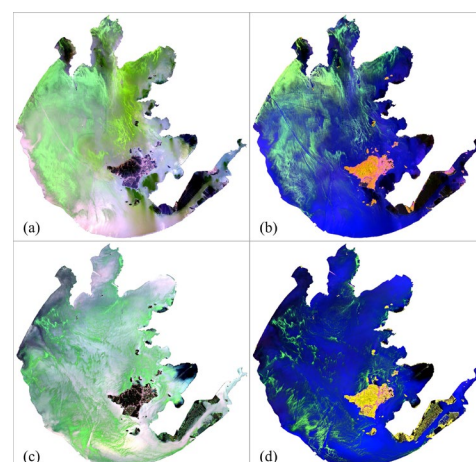


**Figure 1.** Satellite photograph of CBs in Lake Taihu (CHINA). True color images left and false color images right. The characteristic green colors of CBs are visible in (a,b) OLI images (11 May 2017) and (c,d) MSI images (17 August 2019).

## 2. Data and Study Area

### 2.1. Study Area

Lake Taihu ( $30^{\circ}5'N$ – $32^{\circ}8'N$ ,  $119^{\circ}8'E$ – $121^{\circ}55'E$ ) is the third-largest freshwater lake in China, located in a large, heavily urbanized (>40 million inhabitants), and agricultural catchment ( $\sim 36,500 \text{ km}^2$ ) in the Yangtze River Delta region [56]. This typical inland, sizeable shallow lake with an average depth of 1.9 m and a surface area of  $2425 \text{ km}^2$  is characterized by eight major segments from west to east: the west littoral area, the south littoral area, the central lake area, Zhushan Bay, Meiliang Bay, Gonghu Bay, the east littoral area, and the east Taihu Lake (Figure 2). In recent decades, the lake has become increasingly eutrophic [56,57], possibly due to the pollution from agricultural and industrial production, with a long-term increase [58]. At present, the water quality of Lake Taihu is mostly Case IV, and cyanobacteria blooms frequently occur in spring and summer, which seriously threatens the quality of drinking water for millions of people living nearby [59].

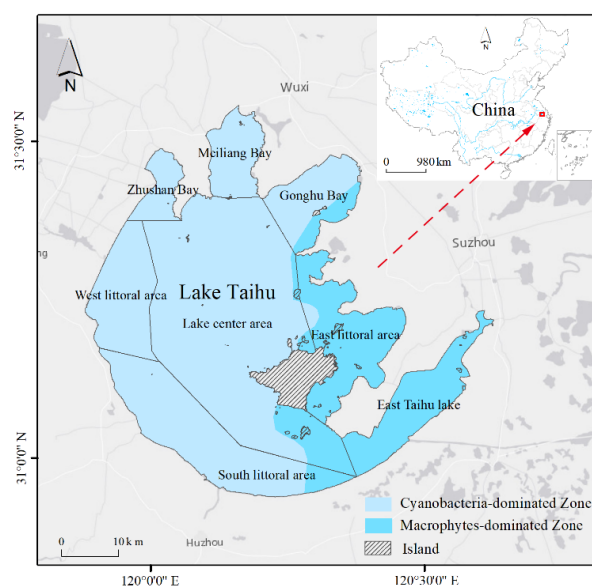


**Figure 2.** Location of Lake Taihu, China. The inset shows that the lake is divided into several lake segments conventionally. Traditionally, cyanobacteria-dominated water in most of the western part and eastern part is dominated by macrophytes.

Traditionally, CBs erupt in most of the western part of Lake Taihu, and the eastern part is dominated by macrophytes with three types of aquatic vegetation [60]. Due to changes in the physical environment (climate warming, decreasing wind speed, increasing water level, and decreasing Secchi disc depth) and human activities, the expansion of CBs in the lake experienced a gradual expansion from Meiliang Bay, Zhushan Bay, and the central lake area, and gradually spread to the eastern lake area [61,62]. Correspondingly, the littoral area of East Taihu Lake was covered with dense aquatic vegetation that extended toward the center of the bay [63]. The infiltration and coexistence of macrophytes and phytoplankton leads to confusion in operational monitoring of CBs because of the similar coloration; for example, both are green or cyan. Complex optical properties with significant spatial and temporal differences [64–66] also make it difficult to identify CBs in the lake.

Alongside Lake Taihu, we used several other eutrophication lakes around the world were to further evaluate the ability of the P-FUI algorithm, such as Lake Chaohu, Dianchi, and Hulun in China, Lesser Slave Lake in Canada, Lake Okeechobee in the United States, Lake Atitlan in Guatemala, Lake Kasumigaura in Japan, Lake Belye in Russia, and Lake Buir in Mongolia. The eastern Gulf of China, with noticeable red tides, was also used for extended evaluation.

## 2.2. In Situ Spectral Data

For this study, the diversity of water samples was considered as much as possible. Due to the effect of human activities, the ecological function of Lake Taihu, Chaohu, Dianchi, and Hulun declined, and a large number of nutrients entered the lakes, resulting in severe eutrophication and frequent outbreaks of CBs [67–70]. The above four lakes are all algae-dominated with different species and amounts. Due to the water exchange with Yangtze and Huaihe River, the water body of Lake Dongting, Poyang, and Hongze have high fluidity and relatively little accumulation of algae [71]. Compared with the previously mentioned lakes, Lake Fuxian seldom experiences an outbreak of algae blooms, which may be due to its deep water and large capacity [72–74].

In order to eliminate the systematic deviation of the hue angle  $\alpha$  of P-FUI in its calculation process, in situ data for the eight lakes were collected from August to November 2020 by field measuring and water sample collection. Cruise measurements were taken as shown in Figure 3, water was sampled in different types of inland waters, and a total of 151 field sampling sites were selected to ensure the representativeness of water bodies. During each cruise, the water-leaving reflectance data were obtained based on the commonly used method [75–77] of using an ASD FieldSpec HandHeld 2 spectroradiometer (ASD, Alpharetta, GA, USA). Subsequently, water samples collected simultaneously with radiometric measurements were immediately transferred to the laboratory for filtration with GF/C filters (Whatman, Maidstone, UK). Then, chlorophyll-a (Chl-a) was extracted and its concentration was quantified to evaluate the effect of Chl-a content on P-FUI, through a procedure given by [78,79], using a UV-2600 Spectrophotometer (Shimadzu, Kyoto, Japan).

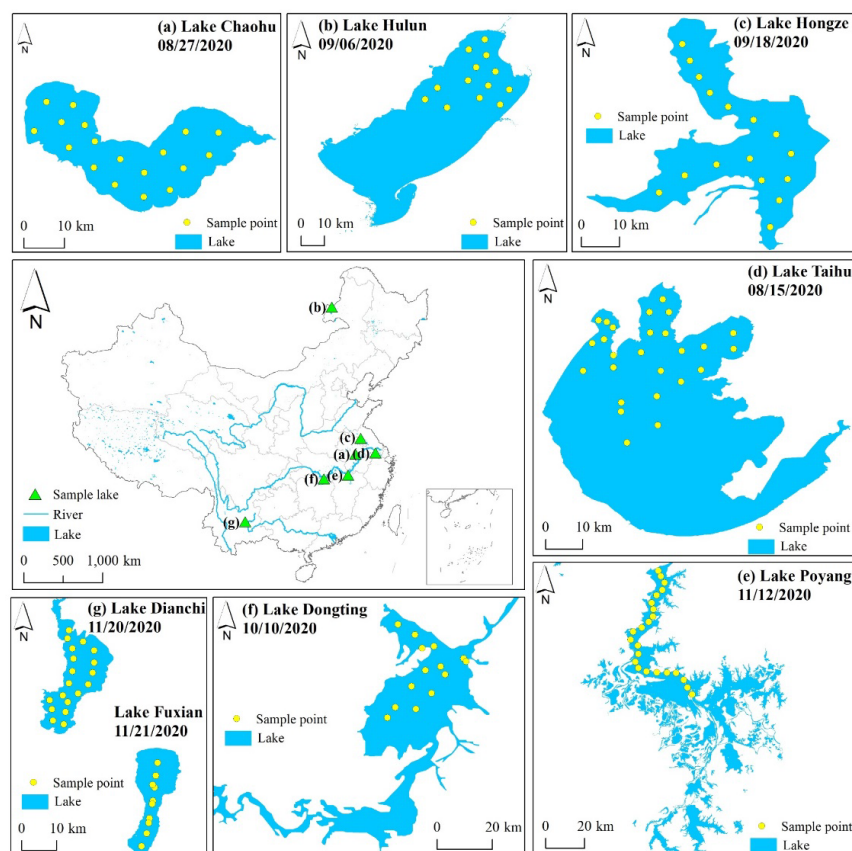


**Figure 3.** Location and date of in situ data in eight lakes, comprising Yangtze River-linked lakes (Lake Poyang, Dongting, and Hongze) and Yangtze River-nonlinked lakes (Lake Taihu and Chaohu) in Yangtze Plain and the Huaihe River Basin, Lake Hulun in Inner Mongolia, and Lake Dianchi and Fuxian in the Yunnan–Guizhou Plateau.

### 2.3. Synthetic Spectral Data

A synthetic remote sensing dataset published by [80] was used to develop the algorithms, which is provided by the International Ocean-Colour Coordinating Group and is generally used as a good benchmark for algorithm development [81]. Details of this dataset can be found in [80] and on the IOCCG website (IOCCG, [https://www.ioccg.org/groups/OCAG\\_data.html](https://www.ioccg.org/groups/OCAG_data.html), accessed on 12 December 2020). This simulated dataset contains 500 synthetic spectra with intrinsic and apparent optical properties of different water components. The data provided every 10 nm between 400 and 800 nm cover a wide range in natural-water composition without errors from measurement procedures, and they have been widely used in the development and verification of water color remote sensing algorithms [46,47,82]. In this study, each spectrum of the dataset was converted to the multiband spectra for the instruments MODIS, OLI, MSI, and OLCI by linear interpolation of the synthetic water-leaving reflectance values at the 10 nm grid. Then, based on the simulated data and in situ measured data, a true color synthesis was performed to correct the hue angle deviation [82], the process of which will be shown later.

### 2.4. Image Pre-Processing

For inter-comparison of the multispectral satellite images, Terra MODIS, Landsat-8 OLI, Sentinel-2 MSI, and Sentinel-3 OLCI images were used to derive P-FUI. Details of the satellite images are given in Table 2. The MODIS\_L1B products were downloaded from the National Aeronautics and Space Administration (NASA, <https://ladsweb.modaps.eosdis.nasa.gov/search/>, accessed on 1 March 2021). Then, bands 3 to 7 of MODIS were resampled to 250 m. Landsat-8 OLI has a 16-day repeat cycle, and its resolution is 30 m for bands 1 to 7. Data are available from <https://earthexplorer.usgs.gov/>, accessed on 20 March 2021. Sentinel-2 MSI and Sentinel-3 OLCI images were obtained from <https://scihub.copernicus.eu/dhus/#/home>, accessed on 5 April 2021. The maximum resolution of MSI images is 10 m, while OLCI images with a resolution of approximately 300 m. For MSI, images of different resolutions were downscaled to 10 m.

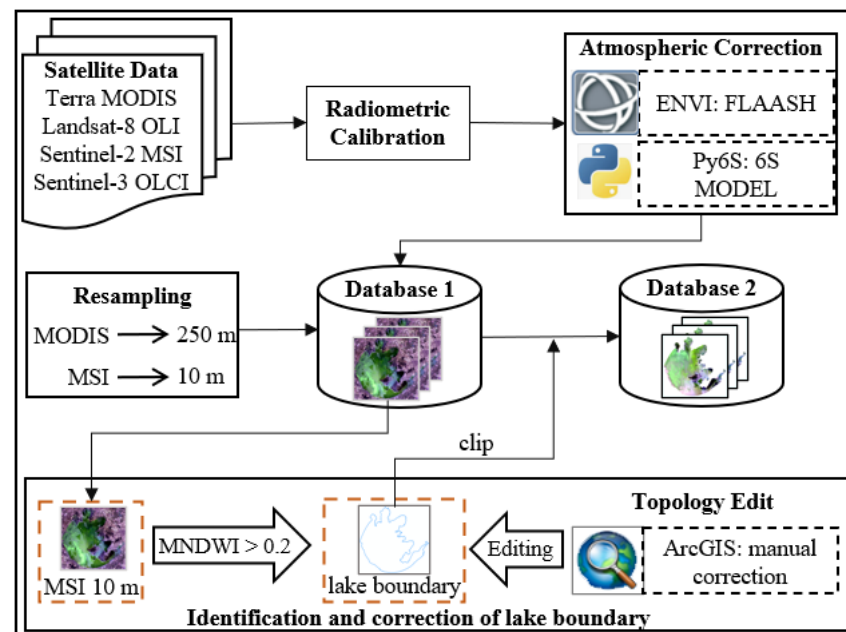
The FLAASH and 6S algorithms were used for atmospheric correction of satellite images in order to perform an inter-comparison. The FLAASH algorithm was processed in ENVI 5.3 software, which is a rigorous method widely used by researchers [83–86]. The 6S algorithm enables accurate simulations of satellite signals from 250 nm to 4000 nm, which accounts for elevated targets, modeling of a realistic molecular/aerosol/mixed atmosphere, use of Lambertian/anisotropic ground surfaces, and calculation of gaseous absorption [87–89]. In this study, 6S corrections were performed using the Py6S python package. This package can be acquired from <https://pypi.org/project/Py6S/>, accessed on 25 May 2021. After pre-processing, which includes radiometric calibration, geometric correction, resampling, and atmospheric correction, the water bodies were extracted using the modified normalized difference water index (MNDWI) [90] based on the MSI images. Equation (1) was applied for water identification:

$$\text{MNDWI} = (R_{\text{GREEN}} - R_{\text{MIR}}) / (R_{\text{GREEN}} + R_{\text{MIR}}) \quad (1)$$

where  $R_{\text{GREEN}}$  and  $R_{\text{MIR}}$  represent the reflectance of the green band and the mid-infrared band, respectively, which correspond to the 3rd and 11th bands for MSI. Then, based on the Otsu algorithm [91,92], the MNDWI threshold of 0.2 was calculated to separate the water and land pixels. Subsequently, topological errors were manually corrected by experts to obtain a more accurate lake boundary, as shown in Figure 4. Concurrent satellite images with cloud cover of less than 10% and CBs were adopted to calculate and evaluate the P-FUI. The nearest satellite image pixels within a  $\pm 3$  h window were used to pair with the in situ data [46].

**Table 2.** Dates and numbers (N) of available satellite images of each lake.

Lakes	Image Time Period				N
	OLI	MODIS	MSI	OLCI	
Lake Taihu	23 October 2013– 22 July 2020	29 November 2013– 28 August 2020	21 April 2019– 25 August 2020	13 September 2016– 20 August 2020	84
Lake Chaohu	19 September 2013	19 October 2019 26 June 2019	19 October 2019 26 June 2019	19 October 2019 14 July 2019	7
Lake Dianchi	28 July 2020 11 August 2019 28 September 2019	8 December 2019 29 October 2019 7 April 2019	8 December 2019 29 October 2019 7 April 2019	8 December 2019 29 October 2019 7 April 2019	12
Lake Hulun	24 July 2017 5 August 2018 21 August 2018	7 September 2020 2 August 2019 19 September 2019	7 September 2020 4 August 2019	7 September 2020 2 August 2020 19 September 2019	11
Beibu Gulf			14 February 2021		1
Lesser Slave Lake	23 September 2013 15 September 2016	28 October 2020 20 October 2020	1 October 2020 16 September 2020	28 October 2020 20 October 2020	8
Lake Okeechobee	2 July 2016 8 August 2018 13 July 2020	15 October 2020 27 September 2020 14 July 2020	15 October 2020 14 July 2020	15 October 2020 27 September 2020 14 July 2020	11
Lake Atitlan	20 August 2015				1
Lake Kasumigaura	1 September 2013				1
Lake Belye	12 September 2014 19 September 2014	8 August 2019 22 July 2019	8 August 2019 22 July 2019		6
Lake Buir	12 July 2015	9 July 2016 6 October 2016			3

**Figure 4.** Flowchart of lake boundary extraction and calibration from satellite images. Database 2 is the final result of image pre-processing. The MNDWI suggested by [90] was used for water body boundary extraction.

### 3. Methods

#### 3.1. Analysis of Spectral Features

In order to evaluate the distinguishability of different surface features of Lake Taihu, typical water spectral features were chosen for analysis. Figure 5 presents the in situ measured spectra of typical water types in Lake Taihu. The spectral curve of clear water shows a peak at the blue-green band, with a gradual decrease to near zero in the near-infrared band [16]. With the intensification of CBs, a significant increase in the near-infrared band appeared due to the increased chlorophyll-a content, which is called a “steep slope effect” [40,93]. Moreover, there are obvious correlations between the concentration of chlorophyll-a and the absorption coefficient near 440 nm and 676 nm, the height of the reflection peak at 700 nm, and the redshift of the peaks from 690 to 740 nm [94–97].

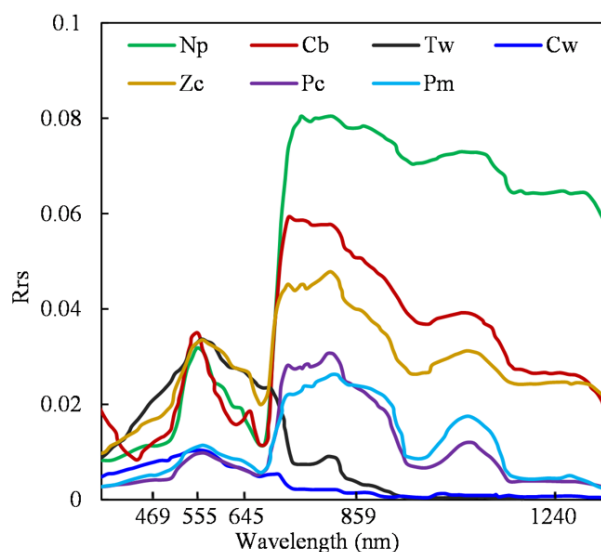


**Figure 5.** In situ measured water surface spectra with typical characteristics of Lake Taihu, featuring *Nymphoides peltatum* (Np), Cyanobacteria blooms (Cb), Turbid water (Tw), Clear water (Cw), *Zizania caduciflora* (Zc), *Potamogeton crispus* (Pc), and *Potamogeton malainus* (Pm).

In order to further analyze the spectral characteristics of CBs, typical land covers of Lake Taihu were visually interpreted based on satellite images. Each spectral curve of the specific surface features is presented in Figure S1. Similar to the in situ measured spectra, the spectral curve of submerged vegetation is similar to clean water in a visible range. For floating-leaf vegetation, noticeable seasonal changes occurred. It grows luxuriantly and densely in summer, covering almost the entire water surface, with a spectral curve close to the typical vegetation, while it is sparser in winter, and the shape of spectra is like that of water bodies and submerged vegetation. The spectral curve of emergent vegetation in spring and autumn is lower than that in summer, especially from near-infrared to short-wave infrared. Compared with other surface features, the spectral curves of CBs are slightly different in the visible range, but more obvious in the near-infrared and short-wave infrared range.

#### 3.2. Pseudo-Forel-Ule Index

In this study, P-FUI was proposed based on satellite data, comprising three parameters: brightness  $Y$ , saturation  $s$ , and hue angle  $\alpha$ . The method of color space conversion was used for P-FUI calculation. Through the different characteristics of spectral curves analyzed above, the bands corresponding to the satellite sensors were divided into three parts: visible light (VIS), near-infrared (NIR), and short-wave infrared (SWIR) range, as shown in Table 3. The water color difference was obtained directly by the method of color space conversion and was used to identify CBs.



**Table 3.** Band division by wavelength range of satellite sensors used in the study.

Sensors	VIS	NIR	SWIR
OLCI	B1-B12	B13-B21	
OLI	B1-B4	B5	B6, B7, B9
MODIS	B1, B3, B4	B2	B5, B6, B7
MSI	B1-B6	B7-B8A, B9	B10, B11, B12

The CIE 1931 XYZ color space is defined mathematically and was created in 1931 by the International Commission on Illumination (CIE) [98]. Tristimulus values X, Y, and Z indicate the comprehensive perception of colors seen by the human eye, with the Y value representing brightness [82,99]. The tristimulus values X, Y, and Z of satellite data were calculated by transforming the color space from RGB to XYZ, which was standardized by CIE special commission as follows [100]:

$$\begin{aligned} X &= 2.7689R + 1.7517G + 1.1302B \\ Y &= 1.0000R + 4.5907G + 0.0601B \\ Z &= 0.0000R + 0.0565G + 5.5934B \end{aligned} \quad (2)$$

According to Table 3, band values of the three divided parts were each assigned to R, G, and B channels. For different sensor types, the combination of bands assigned to R, G, and B channels is different. For sensors with SWIR bands, the band values of VIS, NIR, and SWIR were assigned to B, G, and R channels, respectively. For sensors without SWIR bands, the band values of VIS, NIR, and VIS were assigned to B, G, and R channels, respectively. Then, CIE chromaticity coordinates (x, y) were calculated from the X, Y, and Z by normalizing them to between 0 and 1 (Equation (2)) [101]. Since  $x + y + z = 1$ , the specified color can be determined by the two values of x and y, so the CIE-xy chromaticity diagram (Figure S2) can be used to represent all colors in the visible-light range. Any color corresponds to a unique coordinate (x, y). The intersection of the x- and y-axes is called the white point with the chromaticity coordinate (0.333, 0.333). Its specified spectrum is entirely flat, which means equal power in any wavelength increment of a given size [102].

$$\begin{aligned} x &= \frac{X}{X+Y+Z} \\ y &= \frac{Y}{X+Y+Z} \\ z &= \frac{Z}{X+Y+Z} \end{aligned} \quad (3)$$

The method of calculating hue angle  $\alpha$  has been well proved by [103]. The  $\alpha$  is the angle between the vector to the white point and the negative x-axis in a clockwise direction. The calculation formula is:

$$\alpha = \text{ARCTAN2}(x - 0.333, y - 0.333) \cdot \frac{180}{\pi} \quad (4)$$

where ARCTAN2 is a four-quadrant inverse tangent function that allows  $\alpha$  to range from  $-180^\circ$  to  $180^\circ$ . Since  $\alpha$  would be less than  $-180^\circ$  when  $(x-0.333) < 0$  and  $(y-0.333) < 0$  [82],  $\alpha$  was transformed into  $(\alpha-180^\circ)$  according to [46,103].

In order to simplify the calculation, the saturation s is defined as the distance from any point to the white point in the CIE-xy chromaticity diagram. The calculation formula is as follows:

$$s = \sqrt{(x - 0.333)^2 + (y - 0.333)^2} \quad (5)$$

### 3.3. Hue Angle Correction

The color perceived by the naked eye is a continuous integration in the visible-light range. Due to the discreteness of the band setting in satellite images, there is a systematic deviation  $\Delta$  between the hue angle obtained by the conversion of RGB tristimulus

values and the integration result [82]. Here,  $\Delta$  is defined as the hyperspectral hue angle minus the multispectral hue angle (Equation (5)):

$$\Delta = \alpha_{\text{hyper}} - \alpha_{\text{multi}} \quad (6)$$

where  $\alpha_{\text{hyper}}$  and  $\alpha_{\text{multi}}$  are the results of hyperspectral integration and transformation by tristimulus values based on multispectral, respectively. In order to retrieve the systematic deviation delta ( $\Delta$ ), four steps are required: (1) Through the spectral response function, the IOCCG and in situ measured hyperspectral data are simulated in the corresponding sensor multispectral data, respectively. (2) Based on multispectral data, the hue angle is calculated by methods of color space conversion (Equations (1)–(3)). (3) Tristimulus values X, Y, and Z are calculated according to the spectrophotometry method, and hue angles are obtained. In practice, due to the discreteness of hyperspectral data, summation is often used instead of the integral to simplify the calculation [101]. (4) The deviation delta  $\Delta$  is calculated by using Equation (5), and the delta  $\Delta$  of different sensors is calculated using a specific one-element fifth-order equation according to the equations as shown in Figure 6. Then, add the delta  $\Delta$  to angle  $\alpha$  for correction. A flowchart of obtaining P-FUI is shown in Figure 7.

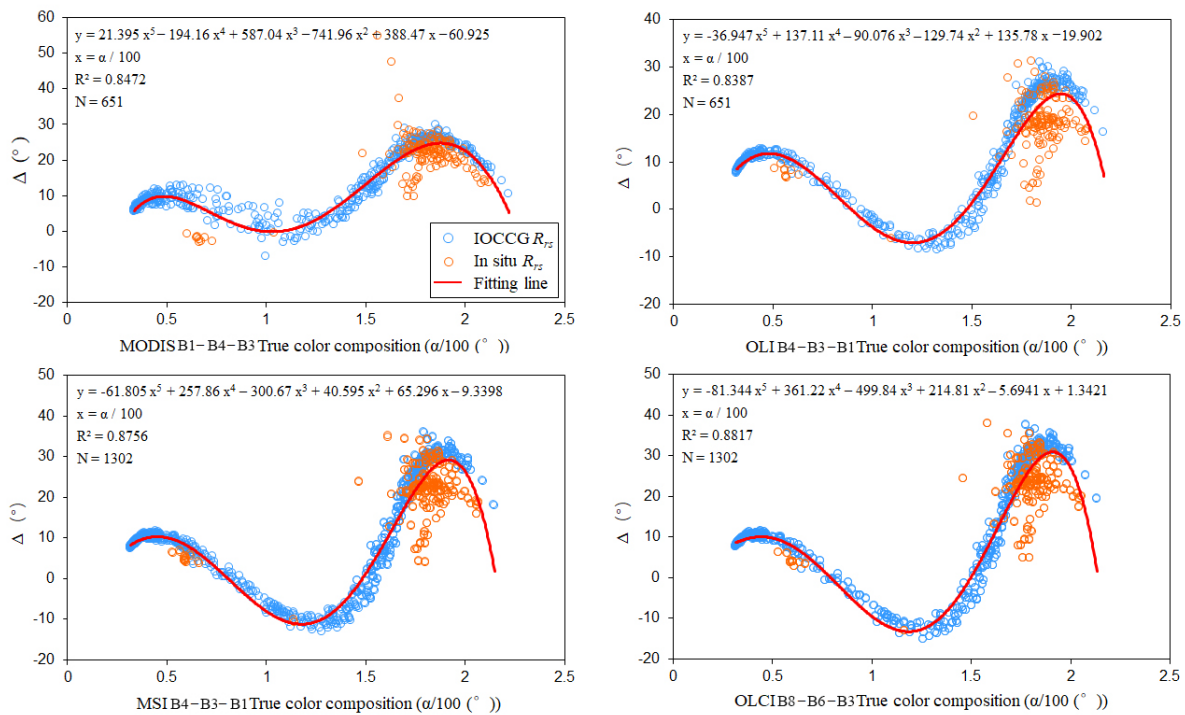


**Figure 6.** Deviation delta  $\Delta$  (°) from the hyperspectral hue angle as a function of satellite image hue angle derived from the linear satellite band combination.

### 3.4. P-FUI Decision Tree

Based on images from MODIS, OLI, MSI, and OLCI satellite sensors, ten typical land covers were visually interpreted, and corresponding chromaticity coordinates were calculated with the distribution shown in Figure 8. The differentiation of the results in the CIE-xy chromaticity diagram of MODIS, OLI, and MSI sensors with SWIR band is better than that of the OLCI sensor without SWIR band.

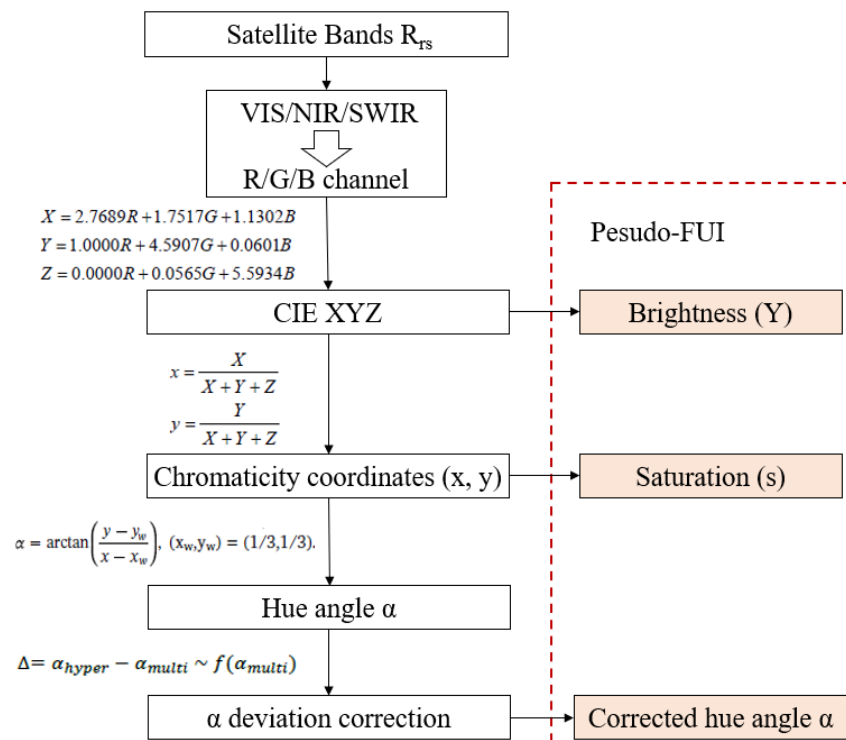


Figure 7. Flowchart of calculating P-FUI from satellite images.

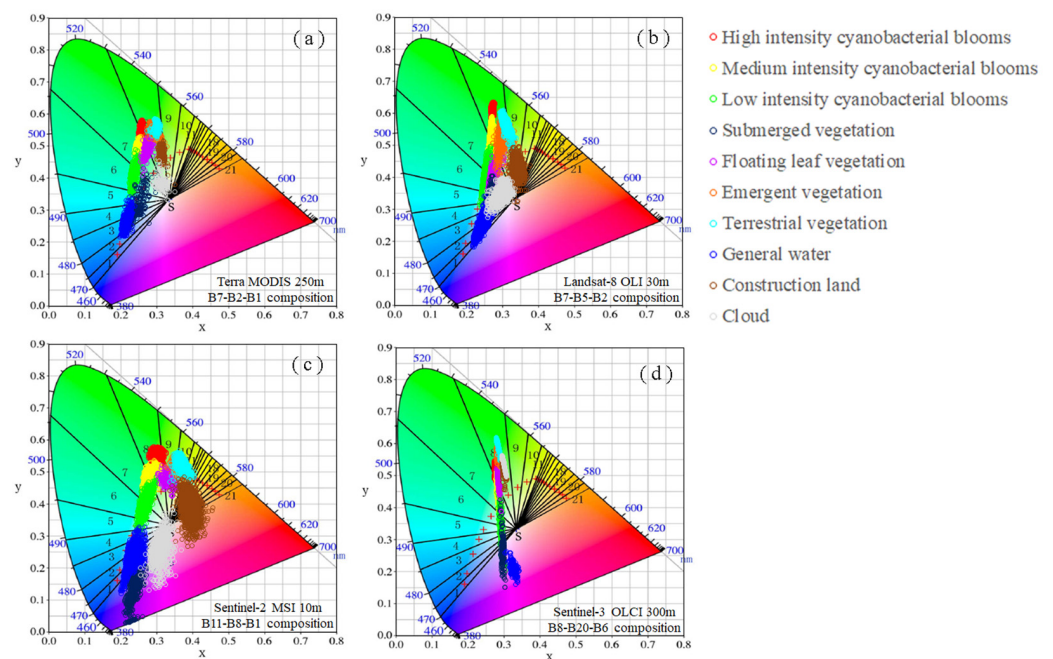
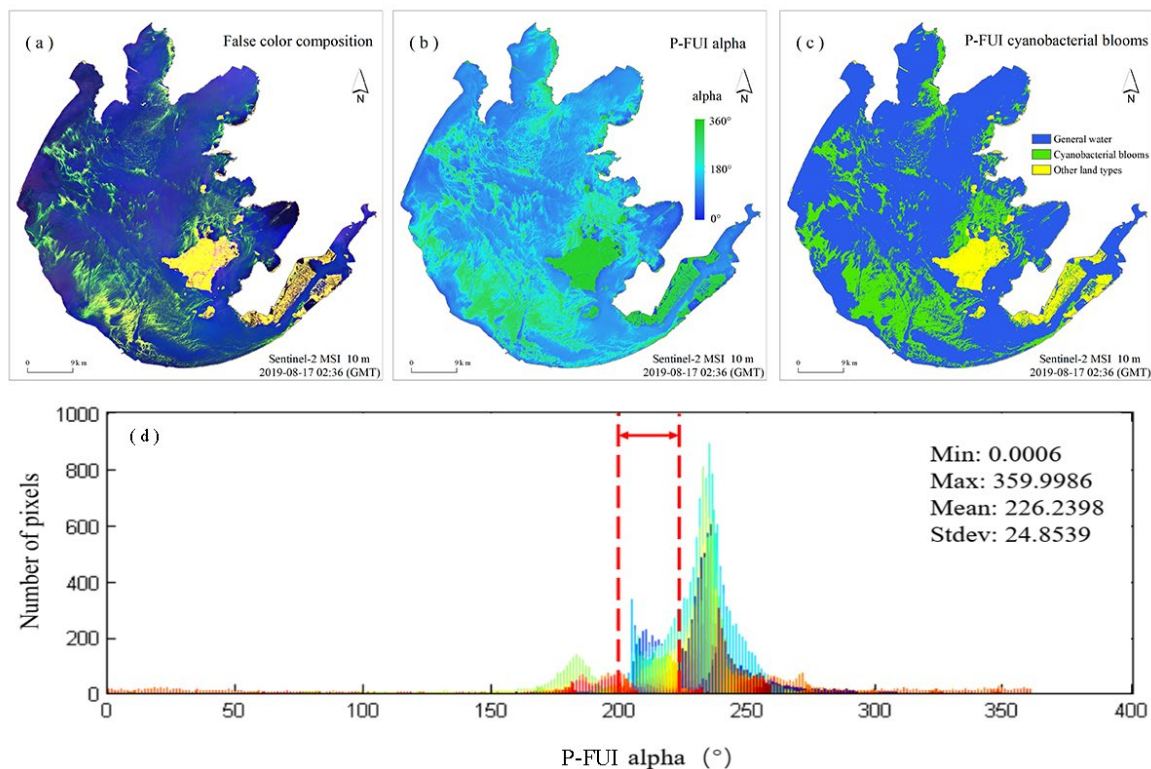


Figure 8. Comparison of the results of chromaticity coordinates of P-FUI calculation based on (a) MODIS, (b) OLI, (c) MSI, and (d) OLCI sensors.

In general, cloud concentrates around the white point and its hue angle is widely distributed, but the saturation is the lowest. The CBs are displayed bright green and blue-green at high intensity and low intensity, respectively, and the color of medium-intensity CBs is between the former two. Terrestrial vegetation and emergent vegetation overlapped to an extent, showing as yellowish-green. Floating leaf vegetation also shows the same color but with lower saturation. Submerged vegetation in the cyan–blue–purple color range

overlaps partially with water bodies. Construction land is concentrated in the range from yellow to orange-red, clearly distinguished from CBs.

Since there are still deficiencies in the identification of CBs when only relying on the P-FUI parameters directly, a decision tree was employed based on the P-FUI's three parameters. Thresholds of the parameters were determined by using a statistical analysis method. Here, the hue angle  $\alpha$  of the P-FUI in Lake Taihu (based on MSI sensor, 17 August 2019) was taken as an example (Figure 9). We calculated the value of  $\alpha$  pixel by pixel and remove outliers; then, the trough of the frequency distribution histogram was selected as the threshold for segmentation of a single image to identify different land covers. Corresponding thresholds of brightness and saturation could also be obtained through the above procedures.



**Figure 9.** Schematic of obtaining the P-FUI alpha threshold based on MSI sensor, with the (a) false color composition, (b) P-FUI hue angle distribution, (c) results of CBs distribution based on hue angle, and (d) threshold frequency distribution histogram of hue angle.

By repeating the threshold retrieved method provided above, the proper intervals of the P-FUI parameters of different land covers could also be determined. Taking the MSI sensor as an example, details of the process using decision trees to identify land covers in Lake Taihu are shown in Figure S3.

### 3.5. Assessment Method

In this study, the three retrieved P-FUI parameters based on satellite data were used through the decision tree. The methods of CBs identification using decision tree were evaluated with the “ground truth” obtained by expert visual interpretation. A total of 296 stratified random sample points were identified using photo-interpretation of the satellite images with the aid of field investigation. Then, the identification results acquired from P-FUI algorithm and expert visual interpretation were comprehensive compared. For

the quantitative assessment, the overall accuracy (OA), producer's accuracy (PA), user's accuracy (UA), and kappa coefficient (KC), defined as follows [104–106], were calculated:

$$OA = \frac{1}{N} \sum_{i=1}^n x_{i,i} \quad (7)$$

$$PA_j = x_{i,i} / \sum_{j=1}^n x_{i,j} \quad (8)$$

$$UA_j = x_{i,j} / \sum_{i=1}^n x_{i,j} \quad (9)$$

$$KC = \frac{N \sum_{i=1}^n X_{ii} - \sum_{i=1}^n (X_{i+} \times X_{j+})}{N^2 - \sum_{i=1}^n (X_{i+} \times X_{j+})} \quad (10)$$

where  $N$  is the total number of samples,  $n$  represents the number of categories,  $x_{i,j}$  represents the element at the intersection of row  $i$  and column  $j$  of the error matrix, and  $X_{i+}$  and  $X_{j+}$  represent the column and row summation of categories, respectively.

## 4. Results

### 4.1. Accuracy Assessment

The identification of CBs and other typical surface features based on P-FUI decision tree, NDVI, EVI, and FAI indices are shown in Figure 10. Compared with NDVI, EVI, and FAI indices, the P-FUI decision tree was better able to distinguish different features, especially CBs from aquatic/terrestrial vegetation. For the MSI sensor, NDVI could identify some terrestrial vegetation on islands with far less accuracy than P-FUI. In addition, it is not sensitive to low-intensity CBs, resulting in a smaller area for low-intensity CBs. Both EVI and FAI have similar misjudgments to NDVI. Neither of them has a proper ability to identify terrestrial and aquatic vegetation, resulting in a more extensive distribution of CBs. Similar to the MSI sensor, the proximate classification results exist for MODIS, OLI, and OLCI sensors.

The results for the quantitative accuracy assessment of CBs identification are shown in Table 4. For MODIS, OLI, MSI, and OLCI sensors, the considerable overall classification accuracy based on the P-FUI decision tree was 98.64%, 97.11%, 93.79%, and 98.33%, respectively, with a kappa coefficient of 0.98, 0.96, 0.91, and 0.98. CBs had producer's accuracy and user's accuracy of more than 94.00% and 94.60%, respectively. Compared with the other three methods, using P-FUI decision tree shows a better performance in identifying CBs. In total, the identification accuracy of CBs using P-FUI decision tree based on multi-source satellite data was satisfactory and has great advantages.

### 4.2. Comparison Validation

#### 4.2.1. Supervised (Unsupervised) Classification Subsubsection

To further evaluate the performance of the P-FUI decision tree, ISODATA clustering and maximum likelihood classification (MLC) were also used to identify CBs for cross-validation based on MSI images. ISODATA clustering is an unsupervised classification method that does not require prior knowledge [45]. In contrast, MLC needs prior category criteria for the process of supervised classification [31]. The results were compared as shown in Figure 11. The ISODATA clustering method misjudges some high-intensity CBs and water bodies as emergent vegetation and low-intensity CBs, respectively, and the consistency with the identification results of P-FUI is 64.55%. For the MLC method, points of interest (POI) of typical features were selected as the input of prior knowledge. Then, various surface features were distinguished better than the ISODATA clustering method, with a consistency of 71.30% compared to the P-FUI decision tree.

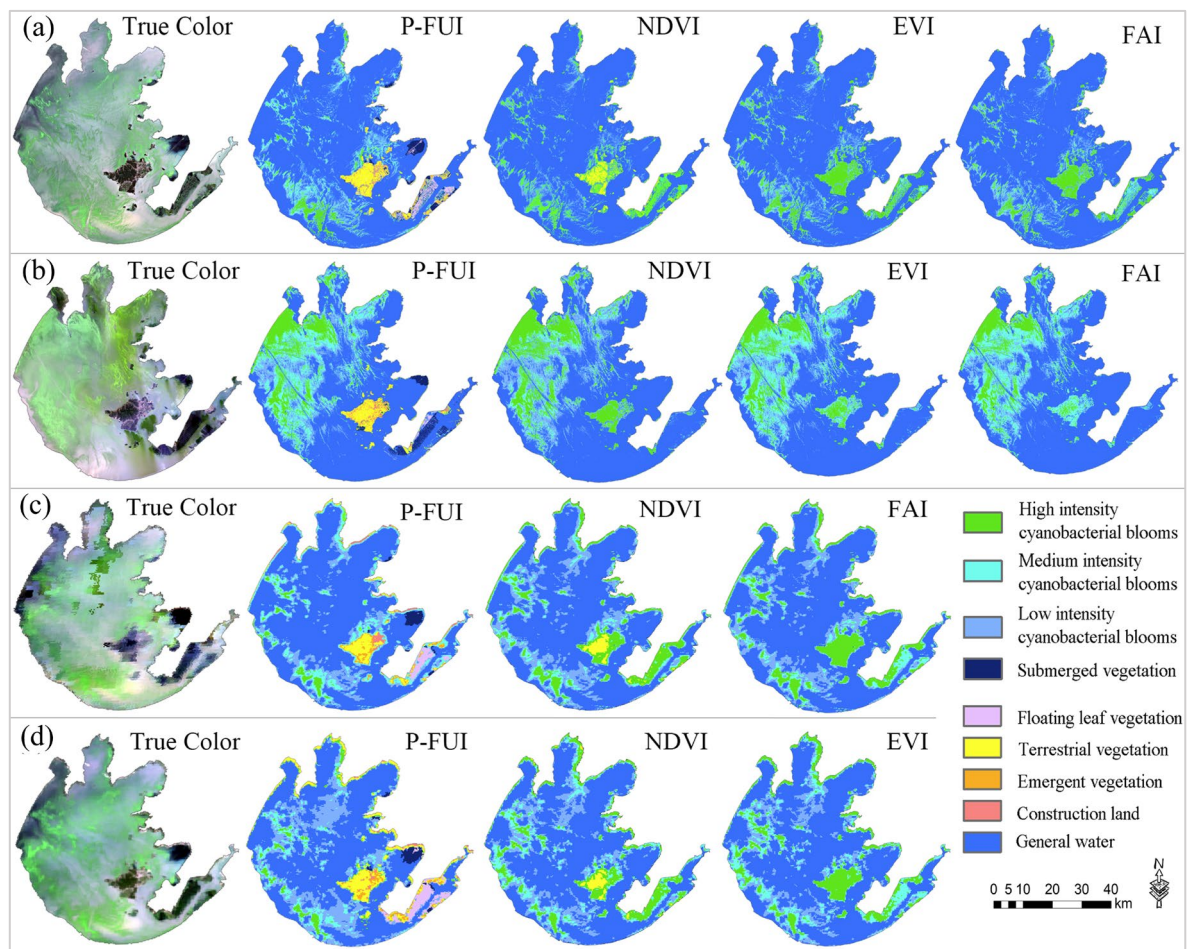


**Figure 10.** Comparison between (a) MSI, (b) OLI, (c) MODIS, and (d) OLCI images of Lake Taihu in identifying surface features under various indexes. The images of MSI, OLI, and MODIS sensors were sensed on 17 August 2019, while the images of the OLCI sensor were sensed on 11 May 2017.

**Table 4.** Quantitative evaluation of the CBs identification accuracy based on MODIS, OLI, MSI, and OLCI sensors.

Sensors	Overall Accuracy	Producer's Accuracy	User's Accuracy	Kappa Coefficient
MODIS				
P-FUI	98.64%	98.65%	98.62%	0.98
NDVI	77.97%	78.04%	80.02%	0.67
FAI	81.14%	81.33%	83.11%	0.72
OLI				
P-FUI	97.11%	96.95%	97.53%	0.96
NDVI	71.17%	72.92%	74.68%	0.57
EVI	81.51%	81.69%	82.35%	0.72
FAI	77.99%	80.00%	79.83%	0.67
MSI				
P-FUI	93.79%	94.00%	94.60%	0.91
NDVI	59.68%	65.89%	61.04%	0.42
EVI	71.71%	74.90%	71.34%	0.58
FAI	64.80%	69.76%	66.18%	0.48
OLCI				
P-FUI	98.33%	98.33%	98.41%	0.98
NDVI	72.99%	73.89%	74.36%	0.59
EVI	68.27%	69.50%	71.86%	0.52

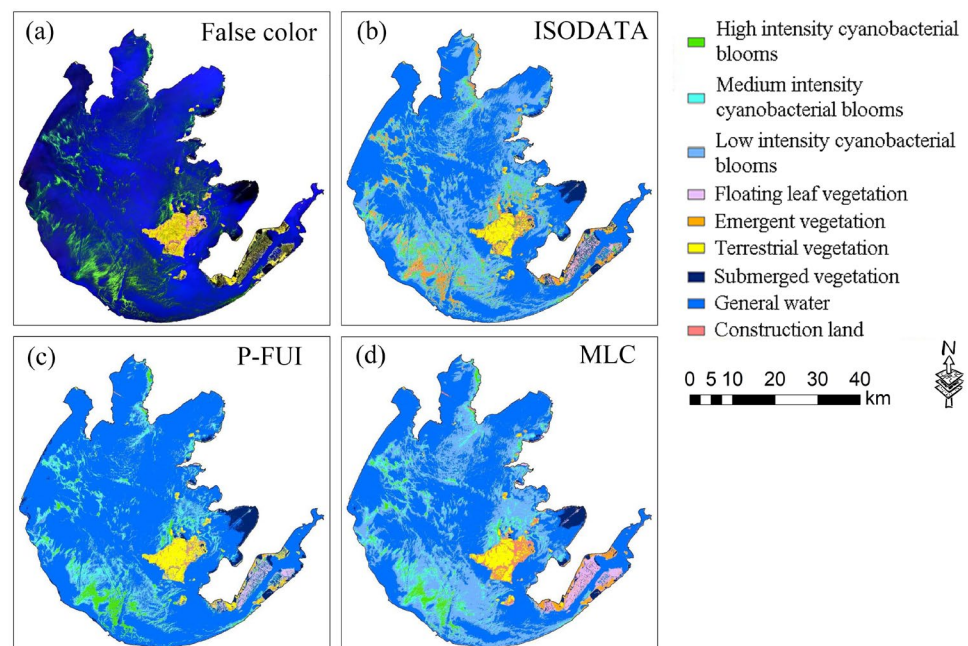


**Figure 11.** Comparison of CBs identification based on (a) false color composition, (b) ISODATA clustering, (c) P-FUI decision tree, and (d) maximum likelihood classification methods.

Statistical analysis was performed to evaluate the classification results of the three methods mentioned above. Compared with ISODATA clustering and MCL methods, the area of identifying low-intensity CBs based on P-FUI decision tree is obviously smaller, while the area of identifying water bodies is larger, which means the former two methods misidentified some water bodies as CBs to an extent. In general, using the P-FUI decision tree to identify CBs has higher accuracy without the need for prior knowledge, which is more convenient and faster.

#### 4.2.2. Multi-Index Decision Tree

Based on the emergent vegetation sensitive index (EVS<sub>I</sub>), FAI, NDVI, and submerged vegetation sensitive index (SVS<sub>I</sub>), [107] constructed a decision tree (hereinafter called the multi-exponential decision tree) for the classification of aquatic vegetation groups and CBs to identify the aquatic plants and CBs in East Taihu Lake. In this study, the P-FUI and multi-exponential decision trees were used to identify CBs based on MSI images. The performances of the two methods were compared (Figure 12). The proportion of the consistent pixels is 83.85%. The inconsistent pixels were mainly distributed in the sparse zone of the floating leaf vegetation area and the submerged vegetation area along the southern coast of East Taihu Lake. In general, the result of the P-FUI decision tree is finer than that of the multi-exponential decision tree.

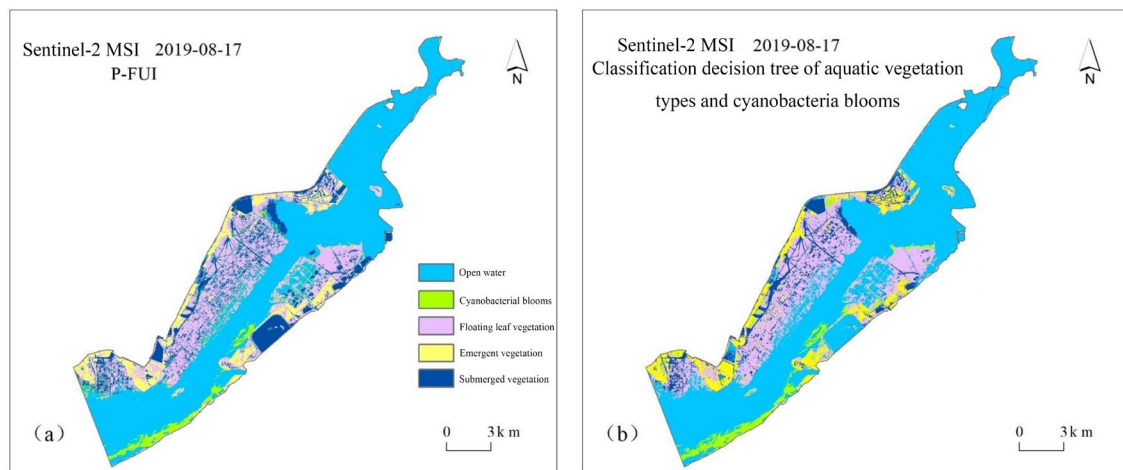


**Figure 12.** Comparison of CBs identification based on (a) P-FUI decision tree and (b) multi-exponential decision tree.

## 5. Discussion

### 5.1. Impact Factors

#### 5.1.1. Cloud Cover

The existence of cloud coverage seriously limits the use of remote sensing data, so cloud removal of satellite imageries is a prerequisite for many remote sensing applications [108,109]. For example, the bloom monitoring based on FAI and NDVI was often disturbed by cloud cover, leading to inaccurate results [110,111]. Although many cloud detection algorithms have been proposed, the preprocessing of cloud coverage is still troublesome in remote sensing applications [112–114].

In this study, the identified results of CBs and clouds based on the OLI images (21 August 2019, Lake Taihu) were compared (Figure S4). The values of NDVI and FAI were extracted by the pixels of CBs and clouds. The histograms showed that the values of NDVI and FAI where CBs and clouds are located have an overlapping area (Figure S4a,b), which indicates that an error in distinguishing occurred when using NDVI and FAI. The surface features identified by the P-FUI algorithm are shown in Figure S4c; the results showed that the cloud coverage and CBs could be well distinguished without cross misjudgment. This means that the preprocessing of cloud coverage in advance is unnecessary in CBs identification based on the P-FUI algorithm, which greatly improved the monitoring efficiency of CBs.

#### 5.1.2. Water Body with High Turbidity

Turbidity can interfere with light emitted by sensors and can thus be an interference in CBs monitoring [115–117]. In order to evaluate the performance of the P-FUI algorithm in identifying CBs in highly turbid water bodies, the spatial distribution of the turbid water index (TWI) in Lake Taihu was obtained based on the MODIS data (18 February 2020) [27]. At the same time, the NDVI and FAI indices were also calculated for inter-comparison (Figure S5). With highly turbid water bodies in the western and southern coastal areas of the lake, the NDVI and FAI indices misidentified water bodies as CBs (Figure S5a,b). Furthermore, the values of NDVI and FAI were extracted by the pixels of CBs and turbid water. The histograms showed an overlapping area between the values of NDVI and FAI, which means that turbid water can easily be misjudged as CBs. In contrast, the spatial distribution of CBs identified by the P-FUI algorithm was consistent with the visual interpretation (Figure S5d), which means that identifying CBs based on P-FUI could effectively avoid the disturbance of turbid water bodies.



### 5.1.3. Chlorophyll-a Concentrations

Chlorophyll-a is a measure of the amount of CB growing in a body of water [36,118]. In order to evaluate the effect of chlorophyll-a content on P-FUI, the concentration of in situ measured chlorophyll-a and the P-FUI parameters calculated from the concurrent MODIS images were used for correlation analysis (Figure S6). The results showed that the hue angle and brightness increased with the concentration of chlorophyll-a, which is consistent with previous studies [119,120]. Both hue angle and brightness have a significantly positive correlation with the concentration of chlorophyll-a at a confidence level of 0.01, and the correlation coefficients are 0.535 and 0.564, respectively. The plots showed that the features overlapped with each other slightly. The reason may be that CBs are susceptible to environmental influences (such as wind) [41], while the spatiotemporal differences of in situ sampling and satellite sensing time did not match exactly. This is also the reason why CBs cannot be identified using a single parameter.

In order to further explore the difference between surface features, the concentration of chlorophyll-a was divided into four types, comprising water bodies and low-intensity, medium-intensity, and high-intensity CBs, with concentrations of 44  $\mu\text{g/L}$ , 352.28  $\mu\text{g/L}$ , 1219.64  $\mu\text{g/L}$ , and 85,763.69  $\mu\text{g/L}$ , respectively. The corresponding mean values of hue angles ( $\alpha$ ) are 69.30°, 98.42°, 141.45°, and 174.44°, and the mean values of brightness ( $Y$ ) are 0.36, 0.65, 1.02, and 1.59, respectively. This is consistent with the blue-green color of CBs, which is an important basis for CBs monitoring, further indicating the reasonable and robust threshold division of P-FUI parameters.

### 5.2. Applicability to New Regions

In order to evaluate the performance of the P-FUI algorithm as it applies to other regions, several lakes mentioned in Section 2.1 were selected for the identification of CBs. Based on satellite images, the visually interpreted features were used as a validation set. Then, the P-FUI algorithm was used to discriminate CBs (Figures S7–S10). The results of identifying CBs based on the OLI and MSI sensors showed a considerable result, with an OA greater than 0.91, and a kappa coefficient of  $\sim 0.90$ . The OA and kappa coefficient based on the MODIS and OLCI sensors were  $\sim 0.87$  and  $\sim 0.86$ , respectively. Although there are slight differences in the accuracy of identifying CBs based on different sensors, the results are still acceptable and even perform well, which indicates that the P-FUI algorithm is highly acceptable in different lakes.

The red tide is caused by the explosive reproduction of plankton, with the abnormal water color being different to the surroundings [121]. Based on the MSI images, the red tides were identified as being in the eastern Gulf of China through the P-FUI algorithm (Figure S11). On the false-color images, red tides appeared as golden or brown bands that were different to the color and shape of the surrounding water bodies. Compared with the visually interpreted features, considerable accuracy was obtained, with OA, kappa coefficient, and F1-score results of 0.87, 0.82, and 0.83, respectively.

### 5.3. Implications for Monitoring Blooms and Protecting Water

The use of remote sensing techniques to identify CBs has a long history. As early as the 1970s, [33] found that some infrared images of Lake Clear in California showed cyanobacterial patterns that could not be observed by traditional limnological techniques, and pointed out that repeated observations could map the movement paths of algae on the water surface. Based on AVHRR image, the ratio vegetation index was developed by [122] to identify the distribution of CBs in Lake Pontchartrain, which was later studied extensively. Subsequently, research on identifying CBs with comprehensive algorithms gradually increased, such as FAI index, AFAl index, decision tree algorithm, and algae pixel-growing algorithm (APA) [21,26,40,123,124]. The common goal of all these algorithms is to realize the efficient identification of CBs with the help of the advantages of remote sensing technology, and to be able to make great progress in daily operational monitoring. However, in practice, none of these methods perform satisfactorily for operational applications. The

possible reasons are inconsistent satellite data, poor robustness of thresholds, and severe interference from factors such as clouds, aquatic vegetation, and highly turbid water bodies.

This paper perfectly fits the current research hotspot of eutrophic lakes. It constructs the P-FUI algorithm which is expected to be applied to CBs business monitoring and to provide services for CBs early warning and the decision-making of management departments. Overall, the success of this effort can be attributed to two factors: (1) this method directly exploits water color differences, which allows it to capture more subtle details of feature differences than traditional methods; (2) the multi-source satellite data make the threshold more robust and the decision tree is used for surface features judgment, which makes the model more reliable and stable. Once the algorithm parameters are further calibrated using related local data, the timely distribution of CBs can be obtained with minimal effort and cost.

From a broader perspective, this approach could be extended to many lakes that are affected by CB problems in the world, providing efficient support for the prevention and control of CBs and the protection of water quality. Under the influence of climate change and high-intensity human activities, the immediate prevention and control of CBs is particularly important to ensure water security. Therefore, it is necessary to make full use of multi-source remote sensing data for effective daily monitoring of CBs in the future.

## 6. Conclusions

A novel algorithm was developed to identify cyanobacterial blooms in a eutrophic lake (Lake Taihu) in China based on MODIS, OLI, MSI, and OLCI images. The decision trees algorithm, namely the P-FUI algorithm, was developed for cyanobacterial blooms identification with a considerable overall accuracy, producer's accuracy, user's accuracy, and kappa coefficient of more than 93.79%, 94.00%, 94.60%, and 0.91, respectively, which is better than traditional cyanobacterial bloom identification methods. The performance was found to be acceptable under nearly all conditions, as the algorithm was shown to be tolerant of perturbations by clouds and high turbidity. Moreover, the findings here were also discussed in terms of the applicability of the P-FUI algorithm to other lakes, and the results showed an acceptable accuracy. It is feasible to identify cyanobacterial blooms and to obtain the classification information of surface features using the P-FUI algorithm. This study provides a new way to map the spatial distribution of cyanobacterial blooms.

**Supplementary Materials:** The following supporting information can be downloaded at: <https://www.mdpi.com/article/10.3390/rs15010215/s1>.

**Author Contributions:** Conceptualization, Y.Z., Z.C. and Y.J.; methodology, Y.Z. and Y.J.; software, Z.C. and Y.J.; validation, Z.C., L.L. and Z.L.; formal analysis, Q.Y.; investigation, Y.Z., Z.C. and Y.J.; resources, Z.C. and Y.J.; data curation, L.L. and Z.L.; writing—original draft preparation, Z.C. and Y.J.; writing—review and editing, Y.Z., Z.C., Y.J., L.L., Z.L. and Q.Y.; visualization, Z.C. and Y.J.; supervision, L.L., Z.L. and Q.Y.; project administration, Y.Z.; funding acquisition, Y.Z. All authors have read and agreed to the published version of the manuscript.

**Funding:** This research was funded by the National Natural Science Foundation of China (Grants No. 42141015 and No. 42171359), the Scientific Instrument Developing Project of the Chinese Academy of Sciences (Grants No. YJKYYQ20200048), and the Water Science and Technology Project of Jiangsu Province (Grants No. 2021032).

**Institutional Review Board Statement:** Not applicable.

**Informed Consent Statement:** Not applicable.

**Data Availability Statement:** Publicly available datasets were analyzed in this study. Terra MODIS data can be found here: [NASA, <https://ladsweb.modaps.eosdis.nasa.gov/search/>, accessed on 1 November 2022]; Landsat-8 OLI data can be found here: [USGS, <https://earthexplorer.usgs.gov/>, accessed on 1 November 2022]; Sentinel-2 MSI and Sentinel-3 OLCI data can be found here: [ESA, <https://scihub.copernicus.eu/dhus/#/home>, accessed on 1 November 2022]. The website registration is open and free to the public.

**Conflicts of Interest:** The authors declare no conflict of interest.

## Abbreviations

P-FUI	Pseudo-Forel-Ule Index;
CBs	Cyanobacterial Blooms;
FAI	Floating Algae Index;
EVI	Enhanced Vegetation Index;
NDVI	Normalized Difference Vegetation Index;
CMI	Cyanobacteria and Macrophytes Index;
TWI	Turbid Water Index;
MNDWI	Modified Normalized Difference Water Index;
VIS	Visible light;
NIR	Near-InfraRed;
SWIR	Short-Wave InfraRed;
ISODATA	Iterative Self-Organizing Data Analysis Techniques Algorithm;
MLC	Maximum Likelihood Classification;
OA	Overall Accuracy;
UA	User's Accuracy;
PA	Producer's Accuracy.

## References

1. Ho, J.C.; Michalak, A.M.; Pahlevan, N. Widespread global increase in intense lake phytoplankton blooms since the 1980s. *Nature* **2019**, *574*, 667–670. [[CrossRef](#)] [[PubMed](#)]
2. Huisman, J.; Codd, G.A.; Paerl, H.W.; Ibelings, B.W.; Verspagen, J.M.; Visser, P.M. Cyanobacterial blooms. *Nat. Rev. Microbiol.* **2018**, *16*, 471–483. [[CrossRef](#)] [[PubMed](#)]
3. Song, K.; Fang, C.; Jacinthe, P.-A.; Wen, Z.; Liu, G.; Xu, X.; Shang, Y.; Lyu, L. Climatic versus anthropogenic controls of decadal trends (1983–2017) in algal blooms in lakes and reservoirs across China. *Environ. Sci. Technol.* **2021**, *55*, 2929–2938. [[CrossRef](#)] [[PubMed](#)]
4. Hozumi, A.; Ostrovsky, I.; Sukenik, A.; Gildor, H. Turbulence regulation of Microcystis surface scum formation and dispersion during a cyanobacteria bloom event. *Inland Waters* **2020**, *10*, 51–70. [[CrossRef](#)]
5. Dittmann, E.; Wiegand, C. Cyanobacterial toxins—occurrence, biosynthesis and impact on human affairs. *Mol. Nutr. Food Res.* **2006**, *50*, 7–17. [[CrossRef](#)]
6. Fernandes, S.P.; Kovar, P.; Psenicka, M.; Silva, A.M.; Salonen, L.M.; Espina, B. Selection of covalent organic framework pore functionalities for differential adsorption of microcystin toxin analogues. *ACS Appl. Mater. Interfaces* **2021**, *13*, 15053–15063. [[CrossRef](#)]
7. Sarkar, A.; Rajarathinam, R.; Venkateshan, R.B. A comparative assessment of growth, pigment and enhanced lipid production by two toxic freshwater cyanobacteria *Anabaena circinalis* FSS 124 and *Cylindrospermopsis raciborskii* FSS 127 under various combinations of nitrogen and phosphorous inputs. *Environ. Sci. Pollut. Res.* **2021**, *28*, 15923–15933. [[CrossRef](#)]
8. Zervou, S.-K.; Moschandreou, K.; Paraskevopoulou, A.; Christophoridis, C.; Grigoriadou, E.; Kaloudis, T.; Triantis, T.M.; Tsiaoussi, V.; Hiskia, A. Cyanobacterial Toxins and Peptides in Lake Vegoritis, Greece. *Toxins* **2021**, *13*, 394. [[CrossRef](#)]
9. Brooks, B.W.; Lazorchak, J.M.; Howard, M.D.A.; Johnson, M.-V.V.; Morton, S.L.; Perkins, D.A.K.; Reavie, E.D.; Scott, G.I.; Smith, S.A.; Steevens, J.A. Are harmful algal blooms becoming the greatest inland water quality threat to public health and aquatic ecosystems? *Environ. Toxicol. Chem.* **2016**, *35*, 6–13. [[CrossRef](#)]
10. Jia, T.; Zhang, X.; Dong, R. Long-term spatial and temporal monitoring of cyanobacteria blooms using MODIS on google earth engine: A case study in Taihu Lake. *Remote Sens.* **2019**, *11*, 2269. [[CrossRef](#)]
11. Xu, H.; Paerl, H.W.; Qin, B.; Zhu, G.; Gao, G. Nitrogen and phosphorus inputs control phytoplankton growth in eutrophic Lake Taihu, China. *Limnol. Oceanogr.* **2010**, *55*, 420–432. [[CrossRef](#)]
12. Paerl, H.W.; Otten, T.G. Harmful cyanobacterial blooms: Causes, consequences, and controls. *Microb. Ecol.* **2013**, *65*, 995–1010. [[CrossRef](#)] [[PubMed](#)]
13. Qin, B.; Li, W.; Zhu, G.; Zhang, Y.; Wu, T.; Gao, G. Cyanobacterial bloom management through integrated monitoring and forecasting in large shallow eutrophic Lake Taihu (China). *J. Hazard. Mater.* **2015**, *287*, 356–363. [[CrossRef](#)]
14. Millie, D.F.; Weckman, G.R.; Young II, W.A.; Ivey, J.E.; Fries, D.P.; Ardjmand, E.; Fahnenstiel, G.L. Coastal 'Big Data' and nature-inspired computation: Prediction potentials, uncertainties, and knowledge derivation of neural networks for an algal metric. *Estuar. Coast. Shelf Sci.* **2013**, *125*, 57–67. [[CrossRef](#)]
15. Shi, K.; Zhang, Y.; Qin, B.; Zhou, B. Remote sensing of cyanobacterial blooms in inland waters: Present knowledge and future challenges. *Sci. Bull.* **2019**, *64*, 1540–1556. [[CrossRef](#)]

16. Gitelson, A.A.; Dall’Olmo, G.; Moses, W.; Rundquist, D.C.; Barrow, T.; Fisher, T.R.; Gurlin, D.; Holz, J. A simple semi-analytical model for remote estimation of chlorophyll-a in turbid waters: Validation. *Remote Sens. Environ.* **2008**, *112*, 3582–3593. [[CrossRef](#)]
17. Gons, H.J.; Auer, M.T.; Effler, S.W. MERIS satellite chlorophyll mapping of oligotrophic and eutrophic waters in the Laurentian Great Lakes. *Remote Sens. Environ.* **2008**, *112*, 4098–4106. [[CrossRef](#)]
18. Hunter, P.D.; Tyler, A.N.; Carvalho, L.; Codd, G.A.; Maberly, S.C. Hyperspectral remote sensing of cyanobacterial pigments as indicators for cell populations and toxins in eutrophic lakes. *Remote Sens. Environ.* **2010**, *114*, 2705–2718. [[CrossRef](#)]
19. Matthews, M.W.; Bernard, S.; Robertson, L. An algorithm for detecting trophic status (chlorophyll-a), cyanobacterial-dominance, surface scums and floating vegetation in inland and coastal waters. *Remote Sens. Environ.* **2012**, *124*, 637–652. [[CrossRef](#)]
20. Stroming, S.; Robertson, M.; Mabee, B.; Kuwayama, Y.; Schaeffer, B. Quantifying the human health benefits of using satellite information to detect cyanobacterial harmful algal blooms and manage recreational advisories in US Lakes. *GeoHealth* **2020**, *4*, e2020GH000254. [[CrossRef](#)]
21. Boardman, J.W. Automating spectral unmixing of AVIRIS data using convex geometry concepts. In Proceedings of the JPL, Summaries of the 4th Annual JPL Airborne Geoscience Workshop, AVIRIS Workshop, Washington, DC, USA, 25–29 October 1993; Volume 1.
22. Kruse, F.A.; Boardman, J.W.; Huntington, J.F. Comparison of airborne hyperspectral data and EO-1 Hyperion for mineral mapping. *IEEE Trans. Geosci. Remote Sens.* **2003**, *41*, 1388–1400. [[CrossRef](#)]
23. Kutser, T.; Metsamaa, L.; Strömbeck, N.; Vahtmäe, E. Monitoring cyanobacterial blooms by satellite remote sensing. *Estuar. Coast. Shelf Sci.* **2006**, *67*, 303–312. [[CrossRef](#)]
24. Quibell, G. Estimating chlorophyll concentrations using upwelling radiance from different freshwater algal genera. *Int. J. Remote Sens.* **1992**, *13*, 2611–2621. [[CrossRef](#)]
25. Cao, M.; Qing, S.; Jin, E.; Hao, Y.; Zhao, W. A spectral index for the detection of algal blooms using Sentinel-2 Multispectral Instrument (MSI) imagery: A case study of Hulun Lake, China. *Int. J. Remote Sens.* **2021**, *42*, 4514–4535. [[CrossRef](#)]
26. Hu, C. A novel ocean color index to detect floating algae in the global oceans. *Remote Sens. Environ.* **2009**, *113*, 2118–2129. [[CrossRef](#)]
27. Liang, Q.; Zhang, Y.; Ma, R.; Loiselle, S.; Li, J.; Hu, M. A MODIS-based novel method to distinguish surface cyanobacterial scums and aquatic macrophytes in Lake Taihu. *Remote Sens.* **2017**, *9*, 133. [[CrossRef](#)]
28. Ali, K.; Witter, D.; Ortiz, J. Application of empirical and semi-analytical algorithms to MERIS data for estimating chlorophyll a in Case 2 waters of Lake Erie. *Environ. Earth Sci.* **2014**, *71*, 4209–4220. [[CrossRef](#)]
29. Lou, I.; Han, B.; Zhang, W. *Advances in Monitoring and Modelling Algal Blooms in Freshwater Reservoirs*; Springer: Berlin, Germany, 2017. [[CrossRef](#)]
30. Kotu, V.; Deshpande, B. Chapter 2—Data Mining Process. In *Predictive Analytics and Data Mining*; Kotu, V., Deshpande, B., Eds.; Morgan Kaufmann: Boston, MA, USA, 2015; pp. 17–36. [[CrossRef](#)]
31. Pasterkamp, R.; Peters, S.; Van Der Woerd, H.; Hoogenboom, H. Detection of algal blooms in the North Sea using supervised classification of SeaWiFS reflectance imagery. In Proceedings of the International Conference on Remote Sensing for Marine and Coastal Environments, Miami, FL, USA, 20–22 May 2002.
32. Shen, L.; Xu, H.; Guo, X. Satellite remote sensing of harmful algal blooms (HABs) and a potential synthesized framework. *Sensors* **2012**, *12*, 7778–7803. [[CrossRef](#)]
33. Wrigley, R.C.; Horne, A.J. Remote sensing and lake eutrophication. *Nature* **1974**, *250*, 213–214. [[CrossRef](#)]
34. Duan, H.; Zhang, S. Cyanobacteria bloom monitoring with remote sensing in Lake Taihu (in Chinese with English abstract). *J. Lake Sci.* **2008**, *20*, 8. [[CrossRef](#)]
35. Gower, J. Red tide monitoring using AVHRR HRPT imagery from a local receiver. *Remote Sens. Environ.* **1994**, *48*, 309–318. [[CrossRef](#)]
36. Choi, J.-K.; Min, J.-E.; Noh, J.H.; Han, T.-H.; Yoon, S.; Park, Y.J.; Moon, J.-E.; Ahn, J.-H.; Ahn, S.M.; Park, J.-H. Harmful algal bloom (HAB) in the East Sea identified by the Geostationary Ocean Color Imager (GOCI). *Harmful Algae* **2014**, *39*, 295–302. [[CrossRef](#)]
37. Peretyatko, A.; Teissier, S.; De Backer, S.; Triest, L. Classification trees as a tool for predicting cyanobacterial blooms. *Hydrobiologia* **2012**, *689*, 131–146. [[CrossRef](#)]
38. Zhu, Q.; Li, J.; Zhang, F.; Shen, Q. Distinguishing cyanobacterial bloom from floating leaf vegetation in Lake Taihu based on medium-resolution imaging spectrometer (MERIS) data. *IEEE J. Sel. Top. Appl. Earth Obs. Remote Sens.* **2017**, *11*, 34–44. [[CrossRef](#)]
39. Mishra, S.; Stumpf, R.P.; Schaeffer, B.A.; Werdell, P.J.; Loftin, K.A.; Meredith, A. Measurement of cyanobacterial bloom magnitude using satellite remote sensing. *Sci. Rep.* **2019**, *9*, 18310. [[CrossRef](#)] [[PubMed](#)]
40. Zhang, Y.; Ma, R.; Duan, H.; Loiselle, S.A.; Xu, J.; Ma, M. A novel algorithm to estimate algal bloom coverage to subpixel resolution in Lake Taihu. *IEEE J. Sel. Top. Appl. Earth Obs. Remote Sens.* **2014**, *7*, 3060–3068. [[CrossRef](#)]
41. Cao, H.; Han, L. Hourly remote sensing monitoring of harmful algal blooms (HABs) in Taihu Lake based on GOCI images. *Environ. Sci. Pollut. Res.* **2021**, *28*, 35958–35970. [[CrossRef](#)] [[PubMed](#)]
42. Jing, Y.; Zhang, Y.; Hu, M.; Chu, Q.; Ma, R. MODIS-satellite-based analysis of long-term temporal-spatial dynamics and drivers of algal blooms in a plateau lake Dianchi, China. *Remote Sens.* **2019**, *11*, 2582. [[CrossRef](#)]
43. Pan, B.; Shi, Z.; An, Z.; Jiang, Z.; Ma, Y. A novel spectral-unmixing-based green algae area estimation method for GOCI data. *IEEE J. Sel. Top. Appl. Earth Obs. Remote Sens.* **2016**, *10*, 437–449. [[CrossRef](#)]

44. Roelfsema, C.; Phinn, S.; Dennison, W.; Dekker, A.; Brando, V. Monitoring toxic cyanobacteria *Lyngbya majuscula* (Gomont) in Moreton Bay, Australia by integrating satellite image data and field mapping. *Harmful Algae* **2006**, *5*, 45–56. [[CrossRef](#)]
45. Zhang, Y.; Hu, M.; Shi, K.; Zhang, M.; Han, T.; Lai, L.; Zhan, P. Sensitivity of phytoplankton to climatic factors in a large shallow lake revealed by column-integrated algal biomass from long-term satellite observations. *Water Res.* **2021**, *207*, 117786. [[CrossRef](#)] [[PubMed](#)]
46. Wang, S.; Li, J.; Zhang, B.; Spyrakos, E.; Tyler, A.N.; Shen, Q.; Zhang, F.; Kuster, T.; Lehmann, M.K.; Wu, Y. Trophic state assessment of global inland waters using a MODIS-derived Forel-Ule index. *Remote Sens. Environ.* **2018**, *217*, 444–460. [[CrossRef](#)]
47. Zhou, Y.; He, B.; Fu, C.; Xiao, F.; Feng, Q.; Liu, H.; Zhou, X.; Yang, X.; Du, Y. An improved Forel–Ule index method for trophic state assessments of inland waters using Landsat 8 and sentinel archives. *GIScience Remote Sens.* **2021**, *58*, 1316–1334. [[CrossRef](#)]
48. Prasad, S.; Saluja, R.; Garg, J. Assessing the efficacy of Landsat-8 OLI imagery derived models for remotely estimating chlorophyll-a concentration in the Upper Ganga River, India. *Int. J. Remote Sens.* **2020**, *41*, 2439–2456. [[CrossRef](#)]
49. Oyama, Y.; Fukushima, T.; Matsushita, B.; Matsuzaki, H.; Kamiya, K.; Kobinata, H. Monitoring levels of cyanobacterial blooms using the visual cyanobacteria index (VCI) and floating algae index (FAI). *Int. J. Appl. Earth Obs. Geoinf.* **2015**, *38*, 335–348. [[CrossRef](#)]
50. Huang, W.; Lou, X. AVHRR detection of red tides with neural networks. *Int. J. Remote Sens.* **2003**, *24*, 1991–1996. [[CrossRef](#)]
51. Shin, J.; Yoon, S.; Cha, Y. Prediction of cyanobacteria blooms in the lower Han River (South Korea) using ensemble learning algorithms. *Desalin. Water Treat* **2017**, *84*, 31–39. [[CrossRef](#)]
52. Hill, P.R.; Kumar, A.; Temimi, M.; Bull, D.R. HABNet: Machine learning, remote sensing-based detection of harmful algal blooms. *IEEE J. Sel. Top. Appl. Earth Obs. Remote Sens.* **2020**, *13*, 3229–3239. [[CrossRef](#)]
53. Qi, L.; Hu, C.; Duan, H.; Cannizzaro, J.; Ma, R. A novel MERIS algorithm to derive cyanobacterial phycocyanin pigment concentrations in a eutrophic lake: Theoretical basis and practical considerations. *Remote Sens. Environ.* **2014**, *154*, 298–317. [[CrossRef](#)]
54. Li, J.; Wu, D.; Wu, Y.; Liu, H.; Shen, Q.; Zhang, H. Identification of algae-bloom and aquatic macrophytes in Lake Taihu from in-situ measured spectra data (in Chinese with English abstract). *J. Lake Sci.* **2009**, *21*, 215–222. [[CrossRef](#)]
55. Wynne, T.T.; Stumpf, R.P.; Tomlinson, M.C.; Dyble, J. Characterizing a cyanobacterial bloom in western Lake Erie using satellite imagery and meteorological data. *Limnol. Oceanogr.* **2010**, *55*, 2025–2036. [[CrossRef](#)]
56. Qin, B.; Paerl, H.W.; Brookes, J.D.; Liu, J.; Jeppesen, E.; Zhu, G.; Zhang, Y.; Xu, H.; Shi, K.; Deng, J. Why Lake Taihu continues to be plagued with cyanobacterial blooms through 10 years (2007–2017) efforts. *Sci. Bull.* **2019**, *64*, 354–356. [[CrossRef](#)]
57. McCarthy, M.J.; Lavrentyev, P.J.; Yang, L.; Zhang, L.; Chen, Y.; Qin, B.; Gardner, W.S. Nitrogen dynamics and microbial food web structure during a summer cyanobacterial bloom in a subtropical, shallow, well-mixed, eutrophic lake (Lake Taihu, China). In *Eutrophication of Shallow Lakes with Special Reference to Lake Taihu, China*; Springer: Berlin, Germany, 2007; pp. 195–207. [[CrossRef](#)]
58. Qin, B.; Xu, P.; Wu, Q.; Luo, L.; Zhang, Y. Environmental issues of lake Taihu, China. In *Eutrophication of Shallow Lakes with Special Reference to Lake Taihu, China*; Springer: Berlin, Germany, 2007; pp. 3–14. [[CrossRef](#)]
59. Duan, H.; Ma, R.; Xu, X.; Kong, F.; Zhang, S.; Kong, W.; Hao, J.; Shang, L. Two-decade reconstruction of algal blooms in China’s Lake Taihu. *Environ. Sci. Technol.* **2009**, *43*, 3522–3528. [[CrossRef](#)] [[PubMed](#)]
60. Luo, J.; Pu, R.; Duan, H.; Ma, R.; Mao, Z.; Zeng, Y.; Huang, L.; Xiao, Q. Evaluating the influences of harvesting activity and eutrophication on loss of aquatic vegetations in Taihu Lake, China. *Int. J. Appl. Earth Obs. Geoinf.* **2020**, *87*, 102038. [[CrossRef](#)]
61. Zhang, Y.; Qin, B.-Q.; Guangwei, Z.H.U. Long-term changes in physical environments and potential implications for the eco-environment of Lake Taihu in the past four decades. *J. Lake Sci.* **2020**, *32*, 1348–1359. [[CrossRef](#)]
62. Zhang, M.; Yang, Z.; Shi, X. Expansion and drivers of cyanobacterial blooms in Lake Taihu. *J. Lake Sci.* **2019**, *31*, 336–344. (In Chinese with English Abstract). [[CrossRef](#)]
63. Zhang, Y.; Liu, X.; Qin, B.; Shi, K.; Deng, J.; Zhou, Y. Aquatic vegetation in response to increased eutrophication and degraded light climate in Eastern Lake Taihu: Implications for lake ecological restoration. *Sci. Rep.* **2016**, *6*, 23867. [[CrossRef](#)]
64. Hu, C.; Lee, Z.; Ma, R.; Yu, K.; Li, D.; Shang, S. Moderate resolution imaging spectroradiometer (MODIS) observations of cyanobacteria blooms in Taihu Lake, China. *J. Geophys. Res. Oceans* **2010**, *115*, C04002. [[CrossRef](#)]
65. Ma, R.; Duan, H.; Lü, C.; Loïselle, S. Unusual links between inherent and apparent optical properties in shallow lakes, the case of Taihu Lake. *Hydrobiologia* **2011**, *667*, 149–158. [[CrossRef](#)]
66. Shi, K.; Zhang, Y.; Liu, X.; Wang, M.; Qin, B. Remote sensing of diffuse attenuation coefficient of photosynthetically active radiation in Lake Taihu using MERIS data. *Remote Sens. Environ.* **2014**, *140*, 365–377. [[CrossRef](#)]
67. Wu, Q.; Xie, P.; Yang, L.; Gao, G.; Liu, Z.; Pan, G.; Zhu, B. Ecological Consequences of Cyanobacterial Blooms in Lakes and Their Countermeasures (in Chinese with English abstract). *Adv. Earth Sci.* **2008**, *23*, 1115. [[CrossRef](#)]
68. Chen, X.; Yang, X.; Dong, X.; Liu, E. Environmental changes in Chaohu Lake (southeast, China) since the mid 20th century: The interactive impacts of nutrients, hydrology and climate. *Limnologia* **2013**, *43*, 10–17. [[CrossRef](#)]
69. Liu, Y.; Chen, J.; Mol, A.P. Evaluation of phosphorus flows in the Dianchi Watershed, southwest of China. *Popul. Environ.* **2004**, *25*, 637–656. [[CrossRef](#)]
70. Zhang, H.; Wang, Q.; Li, G.; Zhang, H.; Zhang, J. Losses of ecosystem service values in the Taihu Lake Basin from 1979 to 2010. *Front. Earth Sci.* **2017**, *11*, 310–320. [[CrossRef](#)]
71. Zhang, G.; Xie, H.; Yao, T.; Kang, S. Water balance estimates of ten greatest lakes in China using ICESat and Landsat data. *Chin. Sci. Bull.* **2013**, *58*, 3815–3829. [[CrossRef](#)]

72. Luo, J.; Yin, J.; Cai, L.; Zhang, K.; Hyde, K.D. Freshwater fungi in Lake Dianchi, a heavily polluted lake in Yunnan, China. *Fungal Divers.* **2004**, *16*, 93–112.
73. Dong, J.; Li, C.; Dai, D.; Yao, S.; Li, S.; Zhou, Q. Seasonal succession of phytoplankton functional groups in Lake Fuxian and its driving factors. *Ann. Limnol. Int. J. Limnol.* **2019**, *55*, 24. [[CrossRef](#)]
74. Liu, W.; Qiu, R. Water eutrophication in China and the combating strategies. *J. Chem. Technol. Biotechnol. Int. Res. Process Environ. Clean Technol.* **2007**, *82*, 781–786. [[CrossRef](#)]
75. Ma, R.; Tang, J.W.; Dai, J.F. Bio-optical model with optimal parameter suitable for Taihu Lake in water colour remote sensing. *Int. J. Remote Sens.* **2006**, *27*, 4305–4328. [[CrossRef](#)]
76. Morel, A.; Prieur, L. Analysis of variations in ocean color. *Limnol. Oceanogr.* **1977**, *22*, 709–722. [[CrossRef](#)]
77. Mueller, J.L.; Morel, A.; Frouin, R.; Davis, C.; Arnone, R.; Carder, K.; Lee, Z.; Steward, R.; Hooker, S.; Mobley, C. *Ocean Optics Protocols for Satellite Ocean Color Sensor Validation, Revision 4. Volume III: Radiometric Measurements and Data Analysis Protocols*; Goddard Space Flight Space Center: Greenbelt, MD, USA, 2003.
78. Ahn, Y.-H.; Shanmugam, P. Derivation and analysis of the fluorescence algorithms to estimate phytoplankton pigment concentrations in optically complex coastal waters. *J. Opt. A Pure Appl. Opt.* **2007**, *9*, 352. [[CrossRef](#)]
79. Jeffrey, S.; Humphrey, G. New spectrophotometric equations for determining chlorophylls a, b, c1 and c2 in higher plants, algae and natural phytoplankton. *Biochem. Und Physiol. Der Pflanz.* **1975**, *167*, 191–194. [[CrossRef](#)]
80. IOCCG. Remote sensing of inherent optical properties: Fundamentals, tests of algorithms, and applications. In *Reports of the International Ocean-Colour Coordinating Group, No. 5*; Lee, Z.-P., Ed.; IOCCG: Dartmouth, NS, Canada, 2006. [[CrossRef](#)]
81. Salama, M.S.; Mélin, F.; Van der Velde, R. Ensemble uncertainty of inherent optical properties. *Opt. Express* **2011**, *19*, 16772–16783. [[CrossRef](#)] [[PubMed](#)]
82. Van der Woerd, H.J.; Wernand, M.R. True colour classification of natural waters with medium-spectral resolution satellites: SeaWiFS, MODIS, MERIS and OLCI. *Sensors* **2015**, *15*, 25663–25680. [[CrossRef](#)]
83. Rani, N.; Mandla, V.R.; Singh, T. Evaluation of atmospheric corrections on hyperspectral data with special reference to mineral mapping. *Geosci. Front.* **2017**, *8*, 797–808. [[CrossRef](#)]
84. Shi, L.; Mao, Z.; Chen, P.; Gong, F.; Zhu, Q. Comparison and evaluation of atmospheric correction algorithms of QUAC, DOS, and FLAASH for HICO hyperspectral imagery. In *Proceedings of the Remote Sensing of the Ocean, Sea Ice, Coastal Waters, and Large Water Regions*, Edinburgh, UK, 26–27 September 2016; p. 999917. [[CrossRef](#)]
85. Efstathiou, M.; Varotsos, C.; Kondratyev, K.Y. An estimation of the surface solar ultraviolet irradiance during an extreme total ozone minimum. *Meteorol. Atmos. Phys.* **1998**, *68*, 171–176. [[CrossRef](#)]
86. Varotsos, C.; Kondratyev, K.Y.; Katsikis, S. On the relationship between total ozone and solar ultraviolet radiation at St. Petersburg, Russia. *Geophys. Res. Lett.* **1995**, *22*, 3481–3484. [[CrossRef](#)]
87. Vermote, E.F.; Tanré, D.; Deuze, J.L.; Herman, M.; Morcette, J.-J. Second simulation of the satellite signal in the solar spectrum, 6S: An overview. *IEEE Trans. Geosci. Remote Sens.* **1997**, *35*, 675–686. [[CrossRef](#)]
88. Vermote, E.; Tanré, D.; Deuzé, J.; Herman, M.; Morcette, J.; Kotchenova, S. Second simulation of a satellite signal in the solar spectrum-vector (6SV). *6s User Guide Version* **2006**, *3*, 1–55. [[CrossRef](#)]
89. Hu, H.; Kang, J.; Zhang, X.; Du, K. Atmospheric correction of SPOT satellite images based on radiation transfer model. In *Proceedings of the 2010 International Conference on Computer Application and System Modeling (ICCASM 2010)*, Taiyuan, China, 22–24 October 2010; pp. V5-188–V185-191. [[CrossRef](#)]
90. Xu, H. Modification of normalised difference water index (NDWI) to enhance open water features in remotely sensed imagery. *Int. J. Remote Sens.* **2006**, *27*, 3025–3033. [[CrossRef](#)]
91. Otsu, N. A threshold selection method from gray-level histograms. *IEEE Trans. Syst. Man Cybern.* **1979**, *9*, 62–66. [[CrossRef](#)]
92. Liao, P.-S.; Chen, T.-S.; Chung, P.-C. A fast algorithm for multilevel thresholding. *J. Inf. Sci. Eng.* **2001**, *17*, 713–727. [[CrossRef](#)]
93. Hu, C.; Muller-Karger, F.E.; Taylor, C.J.; Carder, K.L.; Kelble, C.; Johns, E.; Heil, C.A. Red tide detection and tracing using MODIS fluorescence data: A regional example in SW Florida coastal waters. *Remote Sens. Environ.* **2005**, *97*, 311–321. [[CrossRef](#)]
94. Gower, J. Observations of in situ fluorescence of chlorophyll-a in Saanich Inlet. *Bound. Layer Meteorol.* **1980**, *18*, 235–245. [[CrossRef](#)]
95. Richardson, L.L. Remote sensing of algal bloom dynamics. *BioScience* **1996**, *46*, 492–501. [[CrossRef](#)]
96. Shu, X.; Yin, Q.; Kuang, D. Relationship between Algal Chlorophyll Concentration and Spectral Reflectance of Inland Water (in Chinese with English abstract). *J. Remote Sens.* **2000**, *4*, 41–45. [[CrossRef](#)]
97. Gitelson, A. The peak near 700 nm on radiance spectra of algae and water: Relationships of its magnitude and position with chlorophyll concentration. *Int. J. Remote Sens.* **1992**, *13*, 3367–3373. [[CrossRef](#)]
98. CIE. *Commission Internationale de l’Eclairage Proceedings, 1931*; Cambridge University: Cambridge, UK, 1932; pp. 19–29.
99. Fairman, H.S.; Brill, M.H.; Hemmendinger, H. How the CIE 1931 color-matching functions were derived from Wright-Guild data. *Color Res. Appl.* **1997**, *22*, 11–23. [[CrossRef](#)]
100. Wang, S.; Li, J.; Zhang, W.; Cao, C.; Zhang, F.; Shen, Q.; Zhang, X.; Zhang, B. A dataset of remote-sensed Forel-Ule Index for global inland waters during 2000–2018. *Sci. Data* **2021**, *8*, 26. [[CrossRef](#)]
101. *ASTM Standard E308*; Standard Practice for Computing the Colors of Objects by Using the CIE System. ASTM Headquarters: West Conshohocken, PA, USA, 2006.
102. Kerr, D.A. The CIE XYZ and xyY color spaces. *Colorimetry* **2010**, *1*, 1–16.

103. Wang, S.; Li, J.; Shen, Q.; Zhang, B.; Zhang, F.; Lu, Z. MODIS-based radiometric color extraction and classification of inland water with the Forel-Ule scale: A case study of Lake Taihu. *IEEE J. Sel. Top. Appl. Earth Obs. Remote Sens.* **2014**, *8*, 907–918. [[CrossRef](#)]
104. Congalton, R.G. A review of assessing the accuracy of classifications of remotely sensed data. *Remote Sens. Environ.* **1991**, *37*, 35–46. [[CrossRef](#)]
105. Landis, J.R.; Koch, G.G. The measurement of observer agreement for categorical data. *Biometrics* **1977**, *33*, 159–174. [[CrossRef](#)] [[PubMed](#)]
106. Mboga, N.; Georganos, S.; Grippa, T.; Lennert, M.; Vanhuysse, S.; Wolff, E. Fully convolutional networks and geographic object-based image analysis for the classification of VHR imagery. *Remote Sens.* **2019**, *11*, 597. [[CrossRef](#)]
107. Yang, J.; Luo, J.; Lu, L.; Sun, Z.; Cao, Z.; Zeng, Q.; Mao, Z. Changes in aquatic vegetation communities based on satellite images before and after pen aquaculture removal in East Lake Taihu (in Chinese with English abstract). *J. Lake Sci.* **2021**, *33*, 11. [[CrossRef](#)]
108. Xia, M.; Wang, T.; Zhang, Y.; Liu, J.; Xu, Y. Cloud/shadow segmentation based on global attention feature fusion residual network for remote sensing imagery. *Int. J. Remote Sens.* **2021**, *42*, 2022–2045. [[CrossRef](#)]
109. Karlsen, S.R.; Anderson, H.B.; Van der Wal, R.; Hansen, B.B. A new NDVI measure that overcomes data sparsity in cloud-covered regions predicts annual variation in ground-based estimates of high arctic plant productivity. *Environ. Res. Lett.* **2018**, *13*, 025011. [[CrossRef](#)]
110. Zheng, H.; Liu, Z.; Chen, B.; Xu, H. Quantitative *Ulva prolifera* bloom monitoring based on multi-source satellite ocean color remote sensing data. *Appl. Ecol. Environ. Res.* **2020**, *18*, 4897–4913. [[CrossRef](#)]
111. Kiage, L.M.; Walker, N.D. Using NDVI from MODIS to monitor duckweed bloom in Lake Maracaibo, Venezuela. *Water Resour. Manag.* **2009**, *23*, 1125–1135. [[CrossRef](#)]
112. Mahajan, S.; Fataniya, B. Cloud detection methodologies: Variants and development—A review. *Complex Intell. Syst.* **2020**, *6*, 251–261. [[CrossRef](#)]
113. Xie, F.; Shi, M.; Shi, Z.; Yin, J.; Zhao, D. Multilevel cloud detection in remote sensing images based on deep learning. *IEEE J. Sel. Top. Appl. Earth Obs. Remote Sens.* **2017**, *10*, 3631–3640. [[CrossRef](#)]
114. White, C.H.; Heidinger, A.K.; Ackerman, S.A. Evaluation of Visible Infrared Imaging Radiometer Suite (VIIRS) neural network cloud detection against current operational cloud masks. *Atmos. Meas. Tech.* **2021**, *14*, 3371–3394. [[CrossRef](#)]
115. Ritchie, J.C.; Zimba, P.V.; Everitt, J.H. Remote sensing techniques to assess water quality. *Photogramm. Eng. Remote Sens.* **2003**, *69*, 695–704. [[CrossRef](#)]
116. Zhao, Y.; Liu, D.; Wei, X. Monitoring cyanobacterial harmful algal blooms at high spatiotemporal resolution by fusing Landsat and MODIS imagery. *Environ. Adv.* **2020**, *2*, 100008. [[CrossRef](#)]
117. Gohin, F. Annual cycles of chlorophyll-a, non-algal suspended particulate matter, and turbidity observed from space and in-situ in coastal waters. *Ocean Sci.* **2011**, *7*, 705–732. [[CrossRef](#)]
118. Park, Y.; Lee, H.K.; Shin, J.-K.; Chon, K.; Kim, S.; Cho, K.H.; Kim, J.H.; Baek, S.-S. A machine learning approach for early warning of cyanobacterial bloom outbreaks in a freshwater reservoir. *J. Environ. Manag.* **2021**, *288*, 112415. [[CrossRef](#)]
119. Wernand, M.R.; van der Woerd, H.J.; Gieskes, W.W. Trends in ocean colour and chlorophyll concentration from 1889 to 2000, worldwide. *PLoS ONE* **2013**, *8*, e63766. [[CrossRef](#)]
120. Bielski, A.; Toś, C. Remote Sensing of the Water Quality Parameters for a Shallow Dam Reservoir. *Appl. Sci.* **2022**, *12*, 6734. [[CrossRef](#)]
121. Ramos, C.; Miranda, J.C.; Acum, F.; Pasten, R.; Reyes, R. Red Tide Occurrence and Its Socioeconomic Impacts: Case of the Municipality of Puerto Montt, Chile. *Nat. Hazards Rev.* **2021**, *22*, 04020058. [[CrossRef](#)]
122. Stumpf, R.P.; Tomlinson, M.C. Remote sensing of harmful algal blooms. In *Remote Sensing of Coastal Aquatic Environments*; Springer: Berlin, Germany, 2007; pp. 277–296. [[CrossRef](#)]
123. Fang, C.; Song, K.; Shang, Y.; Ma, J.; Wen, Z.; Du, J. Remote sensing of harmful algal blooms variability for Lake Hulun using adjusted FAI (AFAI) algorithm. *J. Environ. Inf.* **2018**, *34*, 201700385. [[CrossRef](#)]
124. Boardman, J.W. Leveraging the high dimensionality of AVIRIS data for improved sub-pixel target unmixing and rejection of false positives: Mixture tuned matched filtering. In Proceedings of the Summaries of the Seventh JPL Airborne Geoscience Workshop, Pasadena, CA, USA, 12–16 January 1998; pp. 55–56.

**Disclaimer/Publisher’s Note:** The statements, opinions and data contained in all publications are solely those of the individual author(s) and contributor(s) and not of MDPI and/or the editor(s). MDPI and/or the editor(s) disclaim responsibility for any injury to people or property resulting from any ideas, methods, instructions or products referred to in the content.